

## NOVEL METHODS FOR ESTIMATING BANDWIDTH AND STABILITY MARGINS OF PILOT-IN-LOOP SYSTEMS

Dr. Edward Bachelder, [edward.n.bachelder@nasa.gov](mailto:edward.n.bachelder@nasa.gov), San Jose State University Research Foundation/ US Army Aviation Development Directorate, Moffett Field, CA, USA; Bimal Aponso, [bimal.l.aponso@nasa.gov](mailto:bimal.l.aponso@nasa.gov), Aeronautics Projects Office, NASA Ames Research Center, Moffett Field, CA, USA.

### Abstract

A standard metric to estimate system bandwidth is the pilot cutoff frequency, which is the frequency at which the cumulative power ratio of the pilot's control response equals 0.5. Implicit with using the pilot cutoff frequency is that the vehicle output being tracked is approximately the integral of the control input (i.e., rate-commanded). However, errors in estimation will occur when the technique is applied to systems whose tracked outputs differ significantly from this assumption. Furthermore, the type of disturbance spectrum impinging on the tracking task has a strong influence. The effect of these factors on pilot cutoff frequency is examined theoretically, and a method for transforming the cumulative control power ratio is developed that enables the transformed ratio to be applied to any tracked state. A method for determining effective time delay, and effective phase and gain margin from the slope of the transformed cumulative power ratio is also developed. Assuming knowledge of the disturbance spectrum and vehicle dynamics, two techniques are offered to estimate system bandwidth and time delay using: 1) A cutoff frequency (dependent on the forcing function) using the transformed stick response cumulative power ratio; 2) Iteration on the crossover frequency and time delay parameters in the closed-loop Crossover Model until a best match is found between the transformed cumulative power ratios of the modeled and observed stick response. The latter approach does not require that the forcing function contain power extending to or beyond crossover. The development demonstrates that bounding the upper frequency of the computed control power is a critical step of the estimation process, as this reduces the effect of uncorrelated high frequency content arising from sources such as the neuromuscular mode and harmonics of pulse-like control on the estimates. A unique bi-directional spatial filter that allows the frequency and slope from cumulative power ratios to be continuously analyzed when using discrete spectra forcing functions (such as sum-of-sines) is developed. The filter also improves estimation when the forcing spectrum is continuous. A new system bandwidth estimation method that uses the vehicle output cumulative power ratio is proposed, which unlike the cumulative stick power approach does not require an assumption about or measurement of the vehicle dynamics. This technique transforms the output by simple differentiation, allowing similar application of the stick power methods (cumulative power ratio cutoff and model matching). Finally, effective time delay and crossover frequency are estimated using the ideal Crossover Model by matching the observed system time response. The novelty introduced here is that the effective stability margin arising from these two effective parameters closely coincides with the actual system stability margins (phase and gain), irrespective of the differences between the idealized and actual dynamics. This allows the accuracy of any bandwidth estimate to be assessed – establishing the actual bandwidth associated with human-in-loop operation has heretofore proven elusive. The technique lends itself to both manual and automated systems and will be useful for assessing handling qualities. Pilot data from a simulation tracking experiment is used to demonstrate the efficacy of these various estimation techniques.

---

### Copyright Statement

*The authors confirm that they, and/or their company or organization, hold copyright on all of the original material included in this paper. The authors also confirm that they have obtained permission, from the copyright holder of any third party material included in this paper, to publish it as part of their paper. The authors confirm that they give permission, or have obtained permission from the copyright holder of this paper, for the publication and distribution of this paper as part of the ERF proceedings or as individual offprints from the proceedings and for inclusion in a freely accessible web-based repository.*

### 1. INTRODUCTION

Bandwidth and stability margin are fundamental metrics used to evaluate handling qualities. Knowing the bandwidth of the display-pilot-vehicle system is also important for modeling the performance and workload that may result from different designs (i.e., flight controls, automation, display, even pilot control strategy) and task disturbances (i.e. gust turbulence, pilot internal noise). A standard metric that is used to estimate system bandwidth is the pilot cutoff frequency proposed by Tischler [Ref. 1], which is based on the half-power frequency principle. Biernson [Ref. 2]

states that half-power frequency ( $\omega_{hp}$ ) is a bandwidth parameter used to characterize the closed-loop response of a feedback loop. Referring to Figure 1 and Figure 2,  $\omega_{hp}$  is the frequency where the closed-loop magnitude ratio  $|G_{yd}|$  is approximately 70% of the steady-state magnitude ratio (Figure 2a). If the closed-loop power transfer function ( $|G_{yd}|^2$ ) is used,  $\omega_{hp}$  designates the frequency at which the magnitude ratio is 0.5, hence the term “half-power frequency”. The bandwidth parameter for the open-loop response is derived from the loop transfer function crossover frequency  $G_{ye}$ , defined as the frequency where the magnitude ratio  $|G_{ye}|$  is 1 (Figure 2b). The crossover frequency ( $\omega_c$ ) can be considered to be the effective control bandwidth of a feedback-control loop, since it is only at frequencies where the loop gain is greater than unity that the loop provides feedback-control action [Ref. 2].

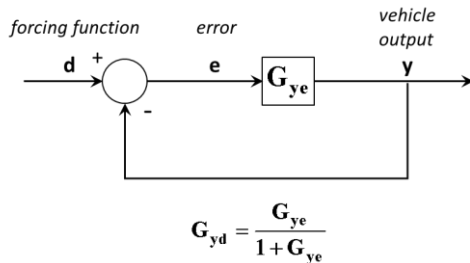


Figure 1. Open-loop and closed-loop transfer functions.

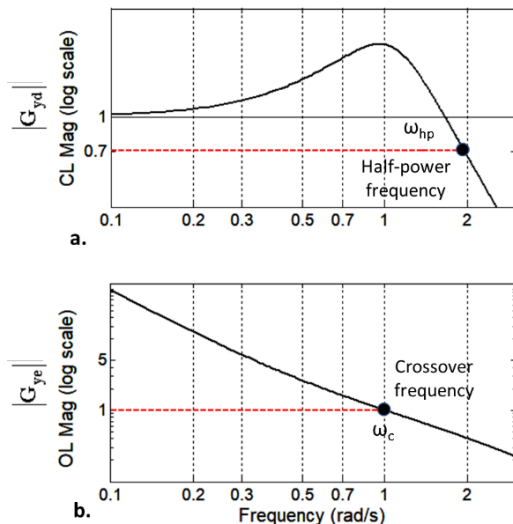


Figure 2. Frequency response plots illustrating definitions of bandwidth parameters: 1) Closed-loop magnitude ratio of  $G_{yd}$ ; 2) Open-loop magnitude ratio of  $G_{ye}$ .

## 2. PILOT CUTOFF FREQUENCY

Tischler’s pilot cutoff frequency ( $\omega_{co}$ ) [Ref. 1] was first used by Atencio [Ref. 3], where it was employed to compare pilot control response in a simulator to executing the same tasks in actual flight. Pilot cutoff frequency is defined as the frequency corresponding to a ratio of cumulative stick power to total stick power (cumulative stick power ratio CSPR, or  $\psi$ ) equal to 0.5:

$$(1) \quad CSPR_{\omega_{co}} = \frac{\frac{1}{2\pi} \int_0^{\omega_{co}} S_{\delta\delta} d\omega}{\frac{1}{2\pi} \int_0^{\infty} S_{\delta\delta} d\omega} = 0.5$$

$S_{\delta\delta}$  is the power spectral density (PSD) of the pilot’s stick signal. Based on the hypothesis that it was analogous to  $\omega_{hp}$ , and the assumption that the pilot acts as a pure gain to the tracking task error [Ref. 1], pilot cutoff frequency was proposed as an estimate of  $\omega_c$  using only stick response data. Various references have used  $\omega_{co}$ , primarily as an estimate of crossover frequency or for pilot workload estimation [Refs. 4, 5, 6, 7].

Three challenges arise when using  $\omega_{co}$ : 1) The original closed-loop bandwidth metric  $\omega_{hp}$  can be an unreliable indicator of actual system bandwidth ( $\omega_c$ ) when the closed-loop system is second-order and oscillatory – human-in-loop operation often falls in this category (shown in the next section); 2)  $\omega_{hp}$  is computed using the known magnitude ratio between the system response and forcing function. Since  $\omega_{co}$  only uses the pilot’s control activity, an assumption must be made about the forcing function spectrum; 3) Assuming knowledge of the forcing function, and that the half-power frequency is a good approximation of system bandwidth, computing  $\omega_{co}$  using the magnitude ratio of pilot control and forcing function would produce the bandwidth of the pilot rather than pilot/vehicle/display system. Only when the vehicle/display suite behaves approximately as an integrator - so that the pilot proportionally responds to tracking error [Ref. 8] – would the bandwidth of the pilot coincide with the system bandwidth ( $\omega_c$ ). This will be addressed in more detail later.

The next section reviews the basic theory of human-in-loop tracking response that will be employed analytically and in simulation to explore these three challenges.

## 3. CROSSOVER MODEL

Figure 3 summarizes McRuer’s Crossover Model [Ref. 8], which effectively states that for single-loop compensatory tracking the pilot will adapt his/her internal dynamics so that the display-pilot-vehicle suite behaves like an integrator with an effective

pure time delay  $\tau$  in the vicinity of crossover frequency ( $\omega_c$ , where the open-loop magnitude is unity, or 0 dB).

$$(2) \quad Y_D Y_P Y_V \approx \frac{\omega_c}{s} e^{-\tau s}$$

Consequently, the error  $e$  roughly commands the rate of the vehicle output  $y$ . Again,  $\omega_c$  corresponds to the system bandwidth, which is the upper frequency that an operator input is effective at reducing tracking error (Figure 4).

Referring to the pilot-in-loop diagram in Figure 3, the closed-loop transfer function is  $G_{yd}$  is

$$(3) \quad G_{yd} = \frac{Y_D Y_P Y_V}{1 + Y_D Y_P Y_V} \approx \frac{\omega_c e^{-\tau s}}{s + \omega_c e^{-\tau s}}$$

For low values of  $\tau$ ,  $G_{yd}$  generates a first-order response. It can be shown that  $G_{yd}$  becomes second-order oscillatory when  $\tau > \frac{1}{e\omega_c}$  [Ref. 8].

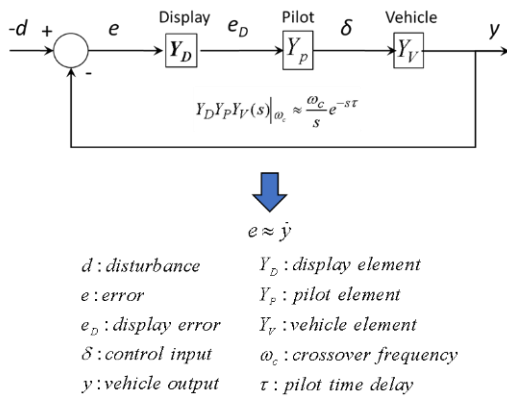


Figure 3. McRuer's Crossover Model.

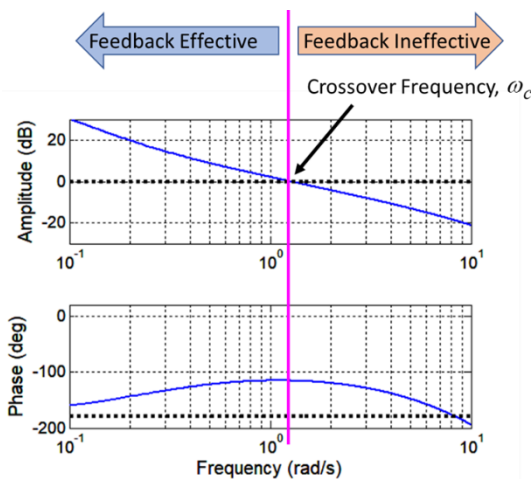


Figure 4. Example open-loop frequency response showing crossover frequency.

Figure 5 shows inverse operator time delay as a function of operator compensation (slope of the

pilot transfer function at crossover frequency). For rate command vehicle dynamics ( $Y_V = \frac{K_V}{s}$ ), the pilot

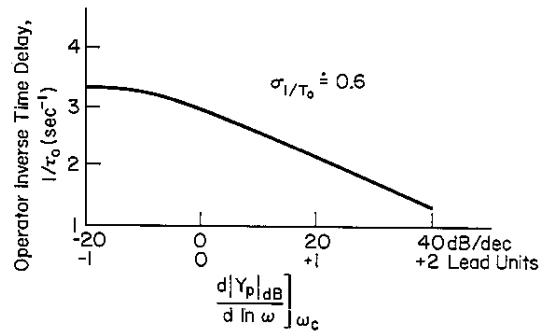


Figure 5. Inverse operator time delay as a function of operator compensation at crossover [Ref. 8].

acts as a pure gain ( $Y_P \approx constant$ ), corresponding to pilot time delay  $\tau \approx 0.3$  seconds. Using a crossover frequency of 2 rad/sec, Figure 6 shows the closed-loop ( $G_{yd}$ ) and open-loop ( $Y_P Y_V$ ) magnitude ratios for two values of  $\tau$ : 0 seconds (unrealistic) and 0.3 seconds (realistic). It is observed that the closed-loop Crossover Model yields  $\omega_c \approx \omega_{hp}$  for near-zero  $\tau$  (Figure 6a), but for realistic time delays  $\omega_{hp}$  can be substantially higher than  $\omega_c$  – for this benign case more than double (Figure 6b). When the vehicle dynamics are more challenging, time delay increases and in general so will system oscillation due to decreasing phase margin [Ref. 8].

#### 4. EQUIVALENT CROSSOVER MODEL SYSTEM

The Crossover Model does not make a distinction between operator, vehicle, or display – the model asserts that in combination these elements behave approximately like an integrator with a transport delay in the vicinity of the crossover frequency. Basic loop closure analysis shows that a pure integrator-like open-loop produces good closed loop command following and stability. The operator is the adaptive element here and adapts to make this so. McRuer proposed a basic pilot crossover model [Ref. 8] consisting of gain, lead, lag, and time delay (Figure 8) as means for adjustment (or compensation). He also introduced a 'Precision' pilot crossover model that included additional terms such as low-frequency lag and a neuromuscular mode. Hess [Ref. 9] proposed his Structural Model which removed the forward path lag and added a proprioceptive feedback loop (first-order lag) around the neuromuscular and feel system elements, further adding precision to the human controller model. Bachelder [Ref. 10] included a pilot dynamic element that accounted for controller

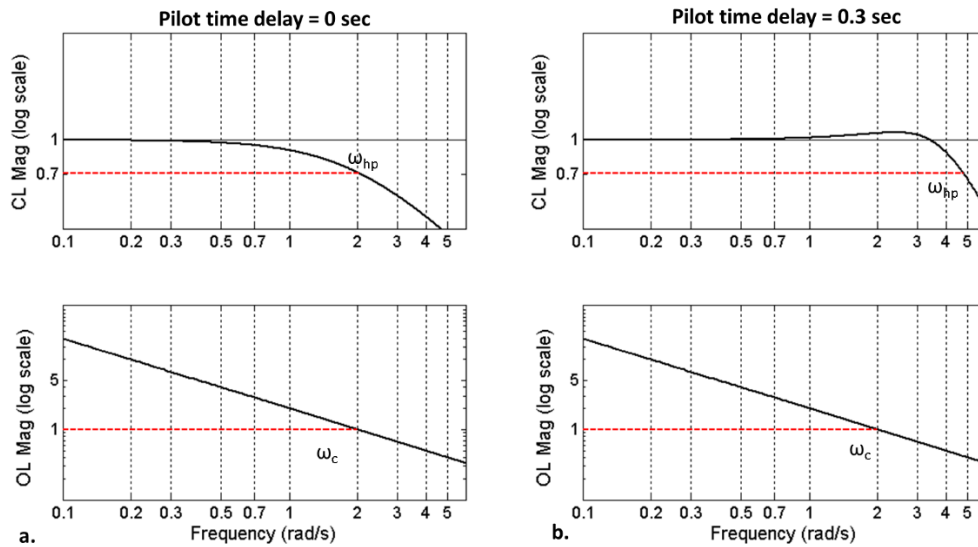


Figure 6. Effect of pilot time delay on  $\omega_{hp}$ : a) No delay; b) 0.3 seconds delay.

technique and could connect to the Structural Model neuromuscular element (during continuous control) or bypass it (i.e., during pulsive control). The Crossover Model has primarily been used to explain or predict pilot compensation associated with a pilot model. It is proposed here that the Crossover Model can be employed to match a system's observed closed-loop response, and the resulting parameters used to estimate the system's actual phase and gain margin.

Phase margin (Figure 7). is defined as the difference between -180 degrees and system phase at gain crossover ( $\omega_{gc}$ , which is also  $\omega_c$ ). Analogously, gain margin is defined as the difference between 0 dB and system gain at phase crossover ( $\omega_{pc}$ , occurring at -180 degrees). Instability theoretically occurs when either margin first reduces to zero.

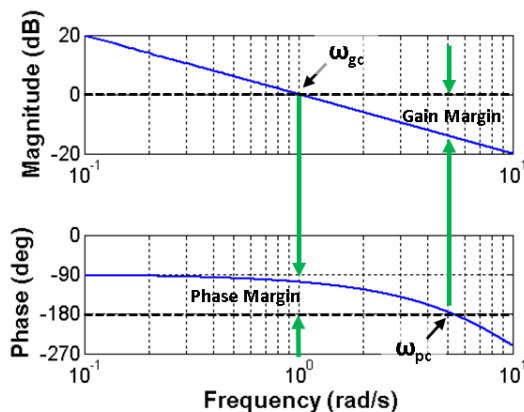


Figure 7. Phase and gain margin examples.

Low-order equivalent systems (LOESs) have been used extensively to characterize aircraft handling

qualities, where high order vehicle dynamics are represented by first and/or second-order transfer functions, and an effective time delay that collectively accounts for the high frequency lags [Ref. 11]. Tischler [Ref. 1] provides practical examples of conducting LOES modeling in the frequency domain using the CIFER<sup>®</sup> identification program. An example of time domain LOES is given in [Ref. 12]. In the current work, the Crossover Model is used as a LOES template of a manually controlled system, and its two parameters adjusted until the closed-loop time response most closely matches the actual observed output (see Figure 8).

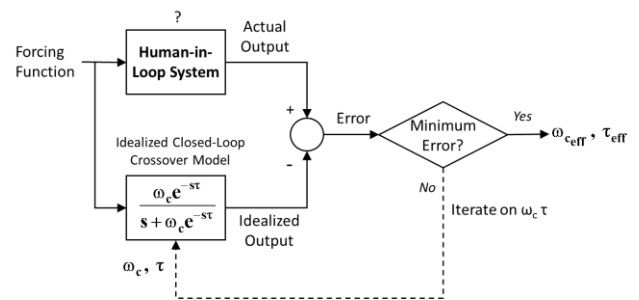
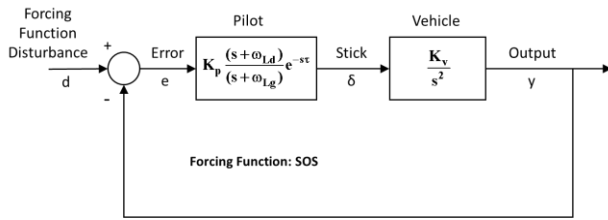


Figure 8. Process for identifying effective crossover and time delay of a human-in-loop system.

Using the process in Figure 8 and simulating a broad range of vehicle dynamics while varying pilot lead/lag compensation and time delay showed that the phase and gain margins computed for the Crossover Model equivalent system closely coincided with the actual phase and gain margins. With few exceptions the effective and actual crossover frequencies matched and the effective time delay primarily served as the adjusting parameter. The next two examples refer to the pilot structure and acceleration-command vehicle

dynamics shown in Figure 9. The basic Crossover pilot model is used, comprised of a gain ( $K_p$ ), lead frequency ( $\omega_{Ld}$ ), lag frequency ( $\omega_{Lg}$ ), and time delay ( $\tau$ ).



**Figure 9. Pilot structure and acceleration-command vehicle dynamics.**

In Figure 10 the crossover frequency is 1 rad/s, and the pilot's lead and lag are far enough from  $\omega_c$  so that there is an extended frequency range around  $\omega_c$  so that the open-loop response resembles a pure integrator (i.e., conforms almost precisely to the ideal Crossover Model). The identified effective system (Figure 10b) is indistinguishable from the actual system (effective and actual time delays are identical). Extended lead over such a wide frequency range is unrealistic in human pilot control.

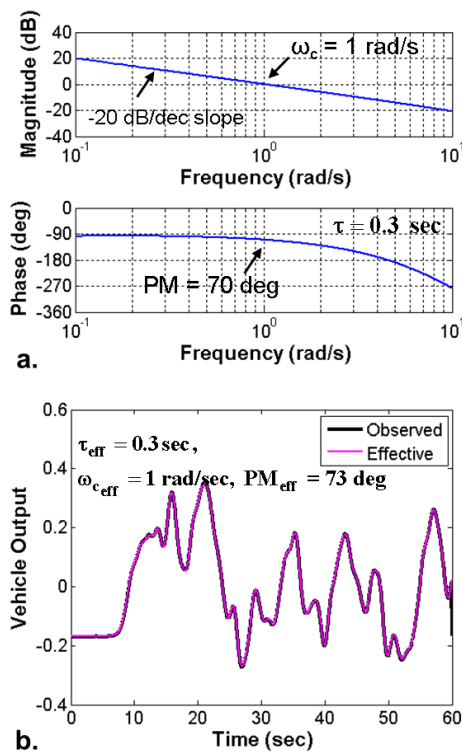


**Figure 10. a) Open-loop frequency response for acceleration-command vehicle (pilot lead  $\omega_{Ld} = 0.01$  and lag  $\omega_{Lg} = 20$  rad/s, far from  $\omega_c = 1$  rad/s); b) Equivalent crossover system output for acceleration command vehicle and observed system output.**

Typically, a human pilot will provide lead compensation over a narrow frequency range in

the crossover region only to the extent needed for stability. In Figure 11  $\omega_c$  remains at 1 rad/s, but the pilot lead and lag occur much closer to  $\omega_c$  so that much of the magnitude slope in the vicinity of  $\omega_c$  differs significantly from the ideal -20dB/decade magnitude slope assumed by the Crossover Model. The identified equivalent system output generally agrees with the actual output, but the effective time delay is almost three times the value of the actual time delay. Effective phase and gain margin are computed using Eq. 4, which are the stability margins associated with the ideal Crossover Model (Ref. <sup>8</sup>). Note gain margin units are decibels ( $20\log_{10}$ ).

$$PM_{eff} = \frac{\pi}{2} - \tau_{eff} \omega_{c,eff}$$

$$(4) \quad GM_{eff}^{dB} = -20\log_{10}\left(1 - \frac{2}{\pi} PM_{eff}\right)$$

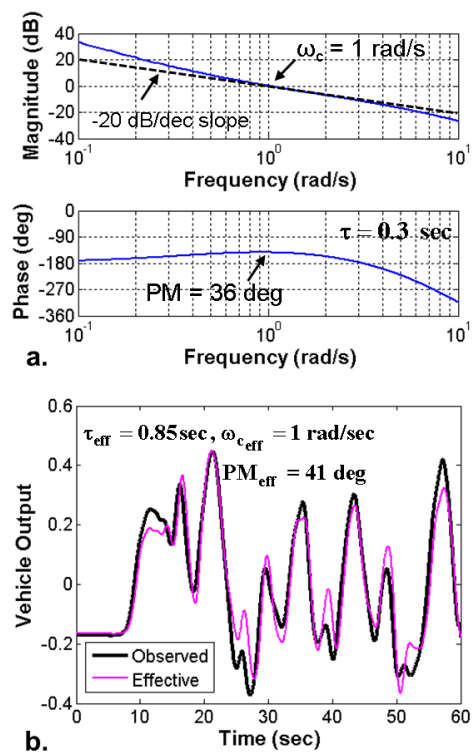


**Figure 11. a) Open-loop frequency response for acceleration-command vehicle (pilot lead  $\omega_{Ld} = 0.5$  and lag  $\omega_{Lg} = 5$  rad/s, close to  $\omega_c = 1$  rad/s); b) Equivalent crossover system output for acceleration command vehicle and observed system output.**

Table 1 compares actual and effective parameter values for the two compensation schemes. Figure 12 compares actual with effective phase margins that were generated by iterating over a range of crossover frequencies (0.5 – 3 rad/s) and pilot time delay (0 – 0.8 sec) using acceleration command vehicle dynamics. Pilot compensation was fixed at  $\omega_{Ld} = 0.1$  rad/s and  $\omega_{Lg} = 10$  rad/s. The Pearson Correlation Coefficient  $R^2$  measure is a metric

**Table 1. Comparison of actual and effective parameter values for two simulated pilot compensation examples.**

	Comp Set A $\left\{ \begin{array}{l} \omega_{L,d} = 0.01 \text{ rad/s} \\ \omega_{L,g} = 20 \text{ rad/s} \end{array} \right.$		Comp Set B $\left\{ \begin{array}{l} \omega_{L,d} = 0.5 \text{ rad/s} \\ \omega_{L,g} = 5 \text{ rad/s} \end{array} \right.$	
	Act	Eff	Act	Eff
$\omega_c$ (rad/s)	1.0	1.0	1.0	1.0
$\tau$ (sec)	0.3	0.3	0.3	0.85
PM (deg)	70	73	36	41
GM (dB)	13	14.5	4.4	5.3

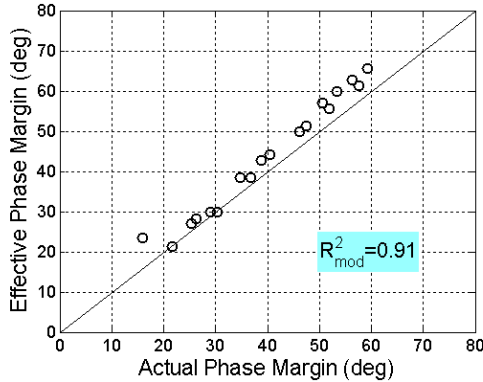


**Figure 12. Comparison of effective and actual phase margins generated by iterating on crossover frequency and pilot time delay (acceleration-command vehicle, pilot lead  $\omega_{L,d} = 0.1$  and lag  $\omega_{L,g} = 10$  rad/s).**

characterizing how well observed outcomes match a best-fit line through the data. However, here the interest is to measure the agreement between an observation ( $Y_{obs}$ ) and an estimate ( $Y_{est}$ ) of that observation' (if agreement was perfect all the points would lie on the line  $y=x$ ). The  $R^2$  metric quantifies the degree of any linear correlation between  $Y_{obs}$  and  $Y_{est}$ , whereas the goodness-of-agreement sought should only consider one specific linear correlation based on  $Y_{est} = Y_{obs}$ . For this,  $R^2$  is modified as shown in Eq 5

$$(5) \quad R_{mod}^2 = 1 - \frac{\sum(X-Y)^2}{\sum X^2}$$

The actual and effective phase margins computed for the iterative simulation show good agreement in Figure 12 ( $R_{mod}^2 = 0.91$ ).

## 5. FORCING FUNCTION SPECTRA

The forcing function (FF) driving the human-in-loop system shown in Figure 13 will have a significant effect on both the pilot and vehicle response. It is key that the assumed FF used to derive relationships between control power and system

bandwidth is consistent with the disturbance that was or will be present when collecting data.

Much of the earlier manual control research used FF's consisting of non-harmonic sum-of-sines [Ref. 8]. The amplitude of the individual sine waves was usually constant out to some shelf frequency, after which the remaining sine wave amplitudes were reduced by 20 dB. The resulting rectangular power spectral density FF permitted important simplification when analytically deriving the association between system response measures (such as stick power) and elements of the Crossover Model. A drawback of this approach is that a rectangular FF is not encountered during actual flight operation. As will be shown, atmospheric gust power spectra resemble second-order lags, with the break generally residing at very low frequency. When there is no gust present (calm winds outdoors, or no gusts used during simulation), the pilot's internal noise will be the driving FF, and this also resembles a second-order lag with the break occurring in the vicinity of  $\omega_c$ .

The following describe four disturbance spectra relevant to manual control research and operation: sum-of-sines, atmospheric turbulence, pilot observation noise, and rectangular.

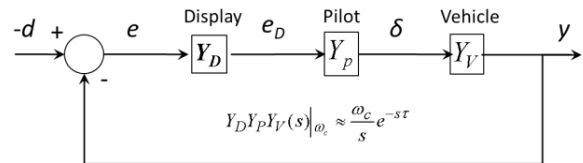


**Figure 13. Block diagram of pilot-in-loop task.**

### 5.1. Sum-of-sines

For a sum-of-sines (SOS) disturbance composed of  $N$  sine waves (non-harmonic frequencies, of amplitude  $A_i$ ) the disturbance PSD given by

$$(6) \quad S_{dd} = \frac{2\pi}{d\omega} \sum_{i=1}^N \frac{A_i^2}{2}$$

where the frequency step-size is denoted by  $d\omega$ .

### 5.2. Atmospheric turbulence

[Ref. 13] describes the Dryden turbulence model, which consists of filters driven by band-limited Gaussian white noise input. Figure 14 gives the model parameters that affect the shape of each axis of gust.

$$\Phi_u(\omega) = \frac{2\sigma_u^2 L_u}{\pi V} \cdot \frac{1}{1+(L_u \frac{\omega}{V})^2}$$

$$\Phi_v(\omega) = \frac{2\sigma_v^2 L_v}{\pi V} \cdot \frac{1+12(L_v \frac{\omega}{V})^2}{[1+4(L_v \frac{\omega}{V})^2]^2}$$

$$\Phi_w(\omega) = \frac{2\sigma_w^2 L_w}{\pi V} \cdot \frac{1+12(L_w \frac{\omega}{V})^2}{[1+4(L_w \frac{\omega}{V})^2]^2}$$

$$2L_w = h$$

$$L_u = 2L_v = \frac{h}{(0.177+0.000823h)^{1.2}}$$

(7)

**Figure 14. PSD spectra for the three linear velocity components [Ref. 14].**

For flight at 100 feet and 60 knots, the break frequency associated with forward velocity gust ( $u$ ) is approximately 0.1 rad/sec. The spectra for all three axes can effectively be treated as double integrators (Eq. 8)

$$(8) \quad S_{dd} \approx \frac{K_g}{\omega^2}$$

The constant  $K_g$  does not affect the computation of CSPR since it appears in both numerator and denominator of the CSPR ratio.

### 5.3. Pilot observation noise

Ref. 8 examined operator control data from various sources to quantify the contribution of noise internal to the operator, referred to as 'observational' noise (added to the error signal that the pilot receives). Figure 15 shows the normalized noise to have a break at approximately 3 rad/sec when no lead is required of the pilot (i.e. vehicle dynamics are rate-command), and a break at approximately 1 rad/sec when pure lead is required

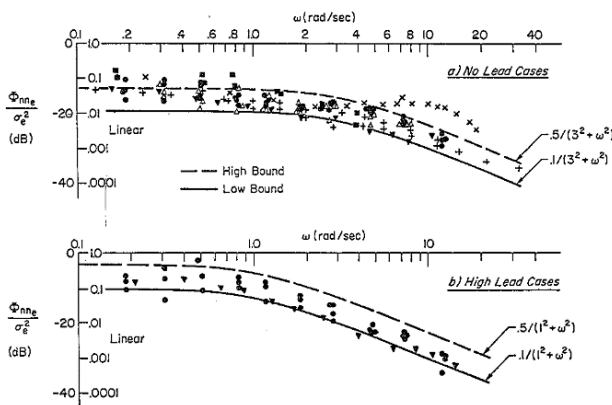


**Figure 15. Normalized observation noise PSD spectra [Ref. 8].**

(i.e. vehicle dynamics are acceleration command). The magnitude of the noise increases with decreasing break frequency. These breaks roughly coincide with  $\omega_c$  so that this spectrum may be generalized as

$$(9) \quad S_{dd} = \frac{K_n}{(\omega^2 + \omega_c^2)}$$

Assigning  $\omega_c$  to the break frequency is a powerful simplification that will allow key insight when this spectrum is examined in the next section.

### 5.4. Rectangular

The rectangular forcing function has often been employed in manual control research, but it neither approximates the gust or the internal noise spectra. It is mainly of interest since it was used for generating much of the earlier data on human operator performance and control. Eq. 10 defines the rectangular spectrum.

$$(10) \quad S_{dd} = \begin{cases} K_r & \omega \leq \omega_d \\ 0 & \omega > \omega_d \end{cases}$$

## 6. CSPR SPECTRAL ANALYSIS USING THE CROSSOVER MODEL AND FORCING FUNCTION SPECTRA

The variance of the stick  $\delta$  can be expressed as

$$(11) \quad \sigma_\delta^2 = \frac{1}{2\pi} \int_0^\infty S_{\delta\delta} d\omega = \frac{1}{2\pi} \int_0^\infty |G_{d\delta}|^2 S_{dd} d\omega$$

where  $G_{d\delta}$  is the transfer function between  $\delta$  and the disturbance  $d$  (Figure 16). Assuming the ideal Crossover pilot (Eq. 2),  $G_{d\delta}$  can be written as

$$(12) \quad G_{d\delta} = \frac{Y_D Y_P}{1 + Y_D Y_P Y_V} = \frac{\omega_c e^{-\tau s}}{(s + \omega_c e^{-\tau s}) Y_V}$$

Substituting into Eq. 11,

$$(13) \quad \sigma_\delta^2 = \frac{1}{2\pi} \int_0^\infty \frac{\omega_c^2}{\omega^2 + \omega_c^2 - 2\omega\omega_c \sin\omega\tau |Y_V|^2} S_{dd} d\omega$$

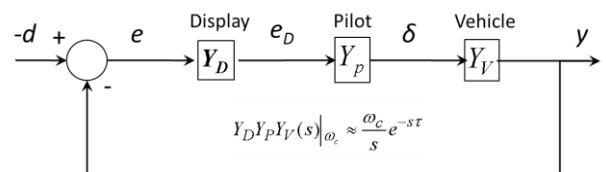


**Figure 16. Closed-loop representation of tracking task.**

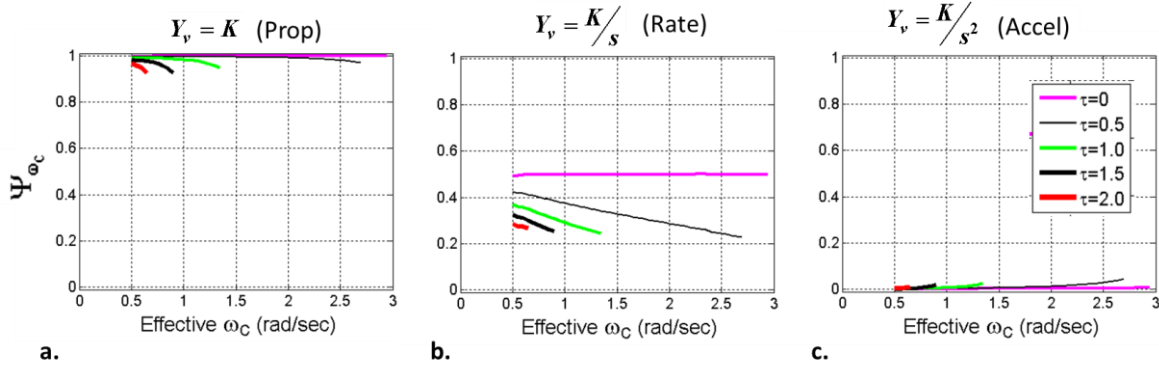


Figure 17. CSPR ( $\psi$ ) values corresponding to effective time delay and crossover frequency (Gust forcing function): a) Proportional control; b) Rate control; c) Acceleration control.

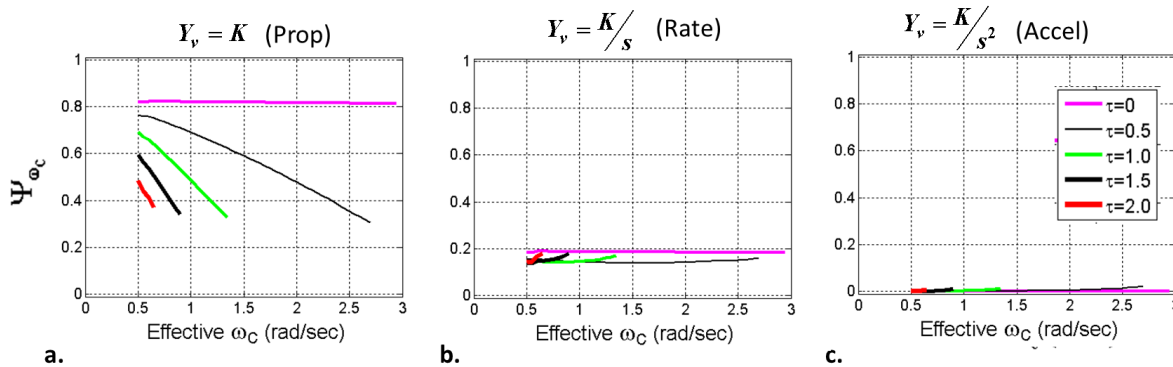


Figure 18. CSPR ( $\psi$ ) values corresponding to effective time delay and crossover frequency (Internal Noise forcing function): a) Proportional control; b) Rate control; c) Acceleration control.

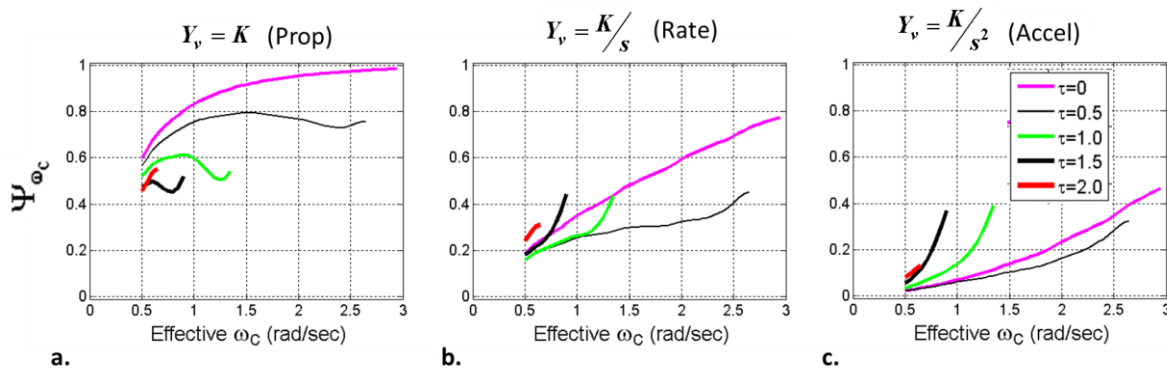


Figure 19. CSPR ( $\psi$ ) values corresponding to effective time delay and crossover frequency (sum-of-sines forcing function): a) Proportional control; b) Rate control; c) Acceleration control.

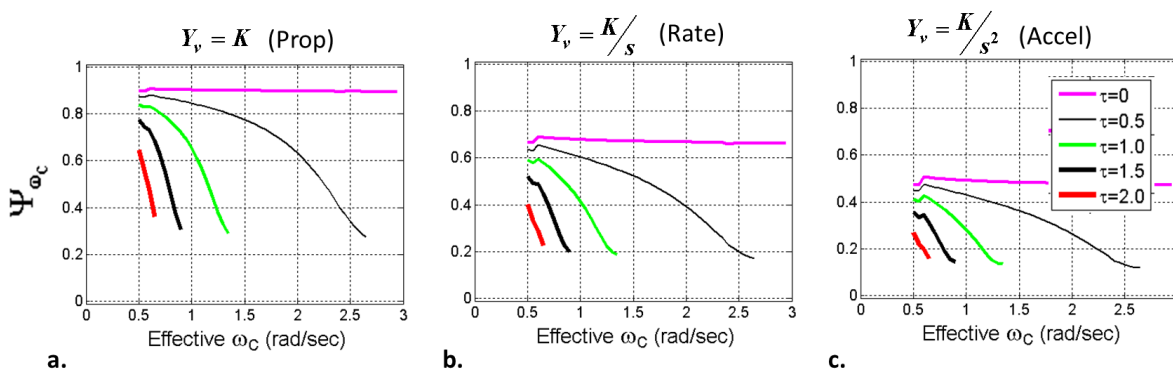


Figure 20. CSPR ( $\psi$ ) values corresponding to effective time delay and crossover frequency (Rectangular forcing function, shelf frequency =  $1.2 \cdot \omega_c$ ): a) Proportional control; b) Rate control; c) Acceleration control.

CSPR computed at  $\omega_c$  is given by

$$(14) \quad CSPR_{\omega_c} = \Psi_{\omega_c} = \frac{\frac{1}{2\pi} \int_0^{\omega_c} S_{\delta\delta} d\omega}{\frac{1}{2\pi} \int_0^{\infty} S_{\delta\delta} d\omega}$$

Three types of vehicle dynamics – proportional ( $Y_v = K_v$ ), rate ( $Y_v = \frac{K_v}{s}$ ), and acceleration command ( $Y_v = \frac{K_v}{s^2}$ ) - were used with Eq. 12 and employ the four disturbance spectra to produce the  $CSPR_{\omega_c}$  responses shown in Figure 17 -Figure 20. The term  $\sin\omega\tau$  in Eq. 13 arising from the pilot time delay prevents a closed-form solution of the integral, requiring either small angle approximation or numerical computation, depending on the application. Looking at the response due to gust using rate command (Figure 17b), it is noteworthy that when  $\tau$  is zero the integral is closed-form and reduces to  $\frac{\tan^{-1}(1)}{\tan^{-1}(\infty)} = 0.5$  (magenta line), which coincides with the value defines pilot cutoff  $\omega_{co}$ . For internal noise ( $\tau = 0$ , rate command),  $CSPR_{\omega_c}$  evaluates exactly to  $\frac{(\frac{\pi}{4} - 0.5)}{\frac{\pi}{2}} = 0.18$  (Figure 18).

Phase margin was limited to a lower limit of 10 degrees, which accounts for the decrease in  $\omega_c$  as  $\tau$  increases. The sum-of-sines spectrum generating the CSPR responses in Figure 19 was of the form  $A_i = \log_{10}(\frac{\beta}{\omega_i})$ , and was also employed in the workload experiment described later.

The shelf frequency ( $\omega_d$  in Eq. 10) used for the rectangular spectrum in Figure 20 was  $\omega_c = 1.2 * \omega_c$ . As  $\omega_d$  increases  $CSPR_{\omega_c}$  will decrease. For  $\omega_d$  values less than  $\omega_c$  will always be unity and meaningless since the upper integration limits in the dividend and divisor of  $CSPR_{\omega_c}$  are both  $\omega_d$ . [Ref. 8] notes that for rectangular spectra pilot performance degrades significantly when  $\omega_d$  approaches or exceeds  $\omega_c$ , (which is the condition that must exist for  $CSPR_{\omega_c}$  to be defined) further reinforcing the unrealism of using the rectangular forcing function in conjunction with  $CSPR_{\omega_c}$ .

$CSPR_{\omega_c}$  is thus highly dependent on the vehicle dynamics and forcing function spectrum, preventing a single CSPR cutoff value from being used for all possible conditions. An alternative approach, developed later, matches the Crossover Model parameters to the observed  $CSPR_{\omega_c}$  response (it is assumed the forcing function is known) enabling identification of not only crossover frequency but also effective pilot time delay. In the next section a transformation that eliminates  $CSPR_{\omega_c}$  variability arising from vehicle dynamics is proposed.

## 7. TRANSFORMING CSPR USING VEHICLE DYNAMICS

As shown in the previous section, vehicle dynamics have a profound effect on CSPR. In general, crossover frequency is found at high, mid-range, and low values of CSPR for proportional, rate, and acceleration command dynamics, respectively. Figure 21 illustrates this using the gust forcing function and the ideal Crossover pilot (exact compensation for vehicle dynamics) with Crossover Model parameters  $\omega_c = 1.5$  rad/s and  $\tau = 0.2$  s. For proportional dynamics CSPR has essentially reached unity before 1 rad/s, providing no useful information in the region of  $\omega_c$ . Conversely, for acceleration command, CSPR has barely begun to increase at 2 rad/s, likewise offering no useful information on  $\omega_c$ . CSPR is therefore not a useful metric for estimating  $\omega_c$  (and neither is  $\tau$ , as will be shown later) when used with

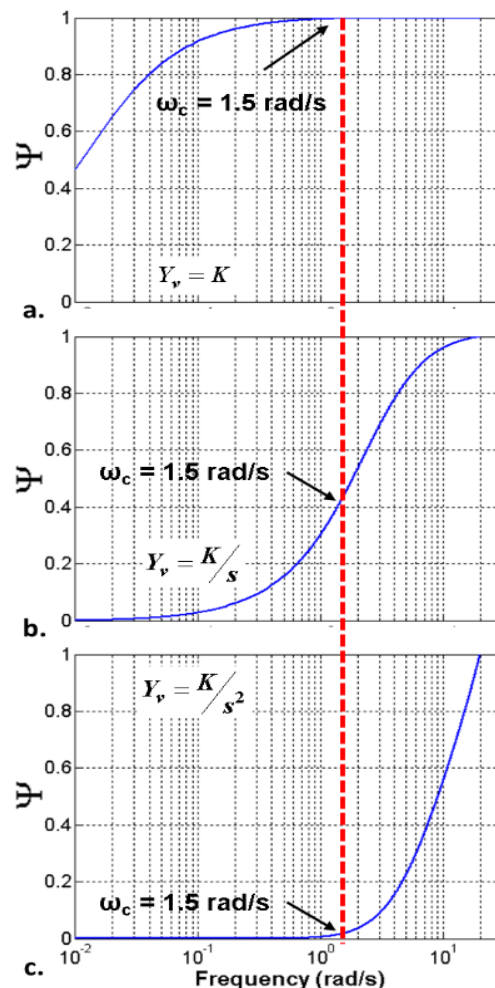


Figure 21. CSPR ( $\psi$ ) responses using the gust spectrum and different vehicle dynamics (ideal Crossover pilot,  $\omega_c=1.5$  rad/s,  $\tau =0.2s$ ): a) Proportional (K); b) Rate (K/s); c) Acceleration (K/s<sup>2</sup>).

these dynamics. However, when rate command dynamics are used (which the pilot cutoff frequency assumes),  $\omega_c$  tends to lie midrange between 0 and 1. It would be ideal if the metric behaved for all vehicle dynamics as it does for rate command. Assuming the pilot  $Y_p$  to be the ideal Crossover pilot (from Eq. 2  $Y_p \approx \frac{\omega_c}{Y_v s} e^{-\tau s}$ ), the transfer function  $G_{d\delta}$  from Eq. 12 can be written as

$$(15) \quad G_{d\delta} = \frac{Y_D Y_P}{1 + Y_D Y_P Y_v} = \frac{s \omega_c e^{-\tau s}}{(s + \omega_c e^{-\tau s}) Y_v s}$$

Note the  $s$  in the numerator and denominator has not been cancelled for ease of manipulation later. Eq. 16 gives  $G_{d\delta}$  for each vehicle type

$$(16) \quad \begin{aligned} G_{d\delta_{prop}} &= K_{prop} \frac{e^{-\tau s}}{(s + \omega_c e^{-\tau s})} \\ G_{d\delta_{rate}} &= K_{rate} \frac{s e^{-\tau s}}{(s + \omega_c e^{-\tau s})} \\ G_{d\delta_{acc}} &= K_{acc} \frac{s^2 e^{-\tau s}}{(s + \omega_c e^{-\tau s})} \end{aligned}$$

The constants  $K_{prop}$ ,  $K_{rate}$ , and  $K_{acc}$  represent  $\frac{\omega_c}{K_v}$ , where  $K_v$  is the constant associated with a vehicle type (i.e.  $Y_v = \frac{K_v}{s}$ ). Substituting the gust forcing function ( $S_{dd} \approx \frac{K_g}{s^2}$ ) and Eq. 15 into Eq. 11 for the three vehicle types,

$$(17) \quad \begin{aligned} \sigma_{\delta}^{2\omega} &= \frac{1}{2\pi} \int_0^{\omega} |G_{d\delta}|^2 S_{dd} d\omega \\ \sigma_{\delta_{prop}}^{2\omega} &= \frac{K_{prop} K_g}{2\pi} \int_0^{\omega} \left| \frac{e^{-\tau s}}{s(s + \omega_c e^{-\tau s})} \right|^2 d\omega \\ \sigma_{\delta_{rate}}^{2\omega} &= \frac{K_{rate} K_g}{2\pi} \int_0^{\omega} \left| \frac{e^{-\tau s}}{(s + \omega_c e^{-\tau s})} \right|^2 d\omega \\ \sigma_{\delta_{acc}}^{2\omega} &= \frac{K_{acc} K_g}{2\pi} \int_0^{\omega} \left| \frac{s e^{-\tau s}}{(s + \omega_c e^{-\tau s})} \right|^2 d\omega \end{aligned}$$

The integral  $\sigma_{\delta_{prop}}^{2\omega}$  in Eq. 17 rapidly approaches its final value because of the free  $s$  in the denominator as demonstrated by CSPR in Figure 21a.  $\sigma_{\delta_{rate}}^{2\omega}$  approaches its final value more slowly, asymptoting after the break frequency  $\omega_c$  (Figure 21b).  $\sigma_{\delta_{acc}}^{2\omega}$  never asymptotes to a final value due to the free  $s$  in the numerator. Figure 21c has a value of one at 20 rad/s only because the integral was only carried out to 20 rad/s. If the integration limit had been 1000 rad/s the initial rise in CSPR would have occurred at a higher frequency than seen in Figure 21c.

In Eq. 16,  $G_{d\delta_{rate}}$  is the stick-to-disturbance transfer function associated with the desirable rate system  $Y_v = \frac{K_v}{s}$ . Effectively the pilot creates a high-pass filter for the forcing function. Comparing this to Eq. 15, it is observed that multiplying  $G_{d\delta}$  by  $Y_v s$

produces the same high-pass filter condition for any vehicle type. This is equivalent to conditioning the stick signal with  $Y_v s$  before it is used in the CSPR computation. The process is shown in Figure 22 and is termed 'stick transformation'.

$$(18) \quad \delta_T(s) = \delta(s) Y_v(s) s$$

The transformed stick is denoted as  $\delta_T$ , and the cumulative stick power ratio denoted as  $CSPR_T$

$$(19) \quad CSPR_T^\omega = \Psi_T^\omega = \frac{\frac{1}{2\pi} \int_0^{\omega} S_{\delta_T} d\omega}{\frac{1}{2\pi} \int_0^{\infty} S_{\delta_T} d\omega}$$

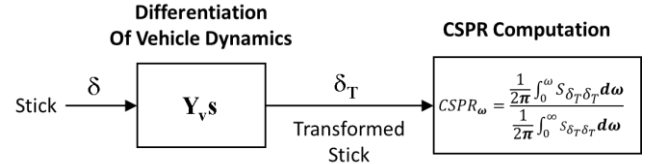


**Figure 22. Stick transformation using differentiated vehicle dynamics.**

The source for the vehicle dynamics  $Y_v$  could come from any of the following: 1) An assumed transfer function; 2) A transfer function fitted through the vehicle frequency response; and 3) The raw vehicle frequency response (interpolating when necessary). When not maneuvering aggressively with large amplitude, vehicle dynamics generally do not change rapidly over time. Vehicle frequency response computed in real time over a period of minutes could thus provide high quality  $Y_v$  for use with the CSPR stick transformation.

In addition to ensuring that CSPR falls within a usable range, the stick transformation eliminates an erroneous assumption that the stick commands the rate of the output being tracked by the pilot (which is the basis for pilot cutoff frequency). In the example shown in Figure 23 the pilot is tracking roll angle, which responds to the stick as an integrated first-order lag. Using the raw stick would result in

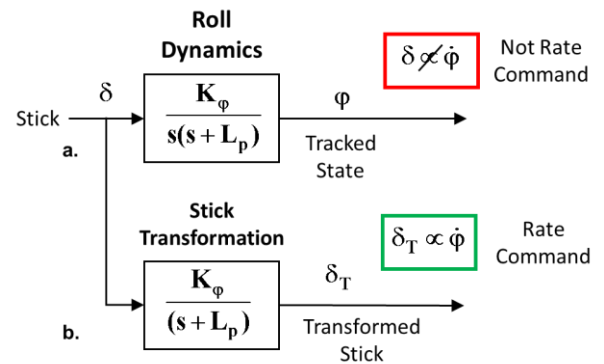


**Figure 23. Roll tracking example: a) Stick produces a tracked state that is not rate commanded ; b) Tracked state is rate commanded with respect to the transformed stick.**

CSPR values greater than those expected for a rate system, whereas employing  $\delta_T$  results in a rate-commanded tracked state relative to the input signal used for  $CSPR_T$ . The stick is transformed by differentiating the roll dynamics (the constant  $K_\varphi$  is irrelevant since it appears in the divisor and dividend of the CSPR ratio and is cancelled out).

## 8. CSPR SPATIAL FILTERING

If the forcing function is stochastic such as atmospheric turbulence, and the time over which stick data is collected is relatively short (i.e., less than a minute) CSPR can exhibit erratic response at the lower frequencies. When sum-of-sines is the forcing function CSPR is a series of steps, which can be problematic when minimizing the difference between observed and modeled CSPR. To address either of these effects, a bi-directional first-order filter was applied to the CSPR signal (Figure 24). The known SOS forcing function  $d$  is used to calibrate the spatial filter. As the length of the time series undergoing Fourier transformation increases, the frequency resolution increases (which will increase the amplitude of the transform). Frequency is treated as time in this filtering scheme. With increasing time series length and amplitude, the same filtering frequency  $\omega_f$  will appear to have a decreasing filtering effect since the ratio of filtered to unfiltered amplitude will be decreasing. To produce the desired filtering effect irrespective of the time series length, the order of  $\omega_f$  is iteratively increased starting from unity until the difference between  $S_{dd}^f$  and  $S_{dd}$  satisfies a minimum threshold.

Figure 25 shows CSPR spatial filtering for two simulated cases (ideal crossover pilot, rate command vehicle, different  $\omega_c$  and  $\tau$ ). The spatial filtering is bi-directional to minimize phase shift normally associated with uni-directional filtering. If the forcing function is not known, the stick input can be used in its place to establish the filter frequency  $\omega_f$ .

## 9. CSPR-CROSSOVER MODEL MATCHING

The transformed stick signal conditions CSPR to behave as if the tracked state was its rate-commanded response. We look now at  $CSPR_T$  used with the forcing functions: gust, internal noise and sum-of-sines (Figure 17 - Figure 19). As previously stated, the rectangular analysis is generally not encountered in practice and is omitted for this discussion. Despite the dependency of  $CSPR_T$  on effective time delay, a single cutoff value (forcing function-specific) based

on an average value may yield satisfactory estimates of  $\omega_c$ , i.e., the set [0.4, 0.18, 0.35] for gust, internal noise and sum-of-sines, respectively. This approach, however, cannot be used if the forcing function's power is too low (or non-existent) prior to the actual crossover frequency.

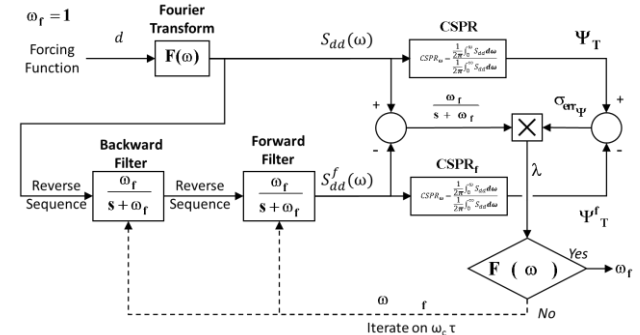


Figure 24. CSPR spatial filter.

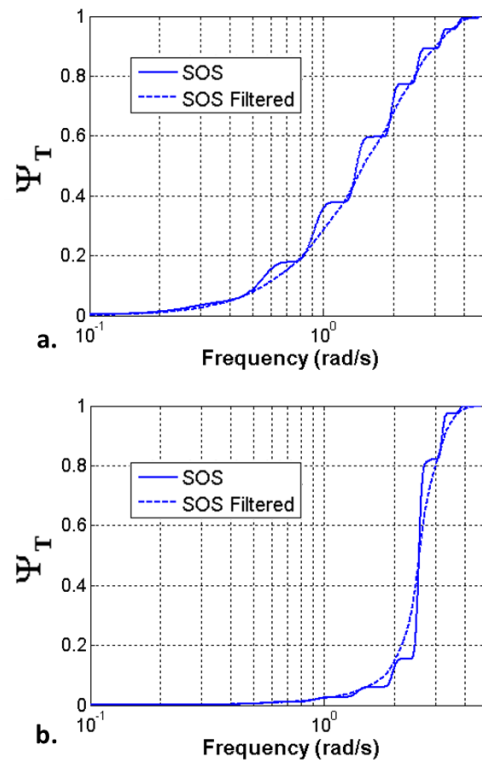


Figure 25. Unfiltered and spatially filtered  $CSPR_T$  ( $\psi_T$ ) ideal Crossover pilot: a)  $\omega_c=1.0$  rad/s,  $\tau=0.3$ s, phase margin=69 deg; b)  $\omega_c=2.5$  rad/s,  $\tau=0.5$ s, phase margin=12 deg.

An alternative approach to a fixed cutoff  $CSPR_T$  frequency is to fit a modeled  $CSPR$  response (based on the idealized Crossover pilot) to the observed  $CSPR_T$  response. A forcing function spectrum is assumed, and there is no requirement for the disturbance to contain power in the vicinity of  $\omega_c$ .

In developing the  $CSPR_T$  model it is efficient to use the transformed stick input. Eq. 15 then becomes

$$(20) \quad G_{d\delta_T} = \frac{s\omega_c e^{-\tau s}}{s + \omega_c e^{-\tau s}}$$

Using  $G_{d\delta_T}$ , Eq. 11 can be re-written as

$$(21) \quad \begin{aligned} \sigma_{\delta_T}^2 &= \frac{1}{2\pi} \int_0^\infty \left| \frac{s\omega_c e^{-\tau s}}{(s + \omega_c e^{-\tau s})} \right|^2 S_{dd} d\omega \\ &= \frac{\omega_c^2}{2\pi} \int_0^\infty \frac{\omega^2}{(\omega^2 + \omega_c^2 - 2\omega\omega_c \sin\omega\tau)} S_{dd} d\omega \end{aligned}$$

As will be discussed later, integrating  $CSPR_T$  out to higher frequencies can include undesirable artifacts created by the pilot, making it necessary to bound the upper frequency with  $\omega_B$ . The modeled  $CSPR_T$  ( $\Psi_{T_{mod}}^\omega$ ) can be expressed as

$$(22) \quad \Psi_{T_{mod}}^\omega = \frac{\frac{1}{2\pi} \int_0^\omega \frac{\omega_c^2 \omega^2}{(\omega^2 + \omega_c^2 - 2\omega\omega_c \sin\omega\tau)} S_{dd} d\omega}{\frac{1}{2\pi} \int_0^{\omega_B} \frac{\omega_c^2 \omega^2}{(\omega^2 + \omega_c^2 - 2\omega\omega_c \sin\omega\tau)} S_{dd} d\omega}$$

where  $\omega_c$  and  $\tau$  are the two unknown parameters used to fit  $\Psi_{T_{mod}}^\omega$  to the observed  $CSPR_T$  ( $\Psi_{T_{obs}}^\omega$ ).

The same set of frequencies resulting from the spectral decomposition of the transformed stick  $\delta_T$

is used to integrate Eq. 22. For consistency the spatial filter that conditions  $S_{\delta_T\delta_T}$  (see Figure 24) is applied to  $\Psi_{T_{mod}}$ . Note that the upper bound frequency  $\omega_B$  employed in  $\Psi_{T_{mod}}$  is also imposed on  $\Psi_{T_{obs}}$  producing a similar effect in both (which washes out during the matching process).

Figure 26 compares the observed  $CSPR_T$  (raw and filtered) with the matched model  $CSPR_T$  (filtered) for two conditions: a)  $\omega_c=0.5$  rad/s,  $\tau=0.3$  sec; b)  $\omega_c=2.5$  rad/s,  $\tau=0.5$  sec. The process of fitting the modeled to observed  $CSPR_T$  is the (frequency domain) analogue of what was done earlier in the time domain to establish an

equivalent crossover model system representation. If the tracking error is known, one could fit  $\frac{\omega_c}{s}$  through the observed open-loop magnitude ratio but assigning an equivalent time delay would be difficult given that phase data associated with human-in-loop operation is generally noisy.

Equivalent crossover model system estimation using  $CSPR_T$  offers several advantages over the traditional frequency response approach usually employed to identify open-loop dynamics: a) An error signal is not required (and often is not available); b) There is less sensitivity to low power in the forcing function ( $CSPR_T$  does not make use of a magnitude ratio that can behave erratically when the divisor approaches zero). When power is low in  $CSPR_T$ , the slope simply decreases (but is never less than zero).

Figure 27 compares estimated (using  $\Psi_{T_{mod}}$ ) with effective crossover frequency, time delay and phase margin using simulated pilot lead  $\omega_{Ld} = 0.01$  rad/s and lag  $\omega_{Lg} = 20$  rad/s (near-ideal Crossover pilot). The sum-of-sines forcing function is employed. Figure 28 compares estimated and actual parameters using simulated pilot lead  $\omega_{Ld} = 0.5$  rad/s and lag  $\omega_{Lg} = 5$  rad/s (non-ideal Crossover pilot). Agreement is very good in both examples. A simulation using the gust spectrum as the forcing function produced similar results, indicating the technique is applicable to both discrete and continuous forcing function spectra.

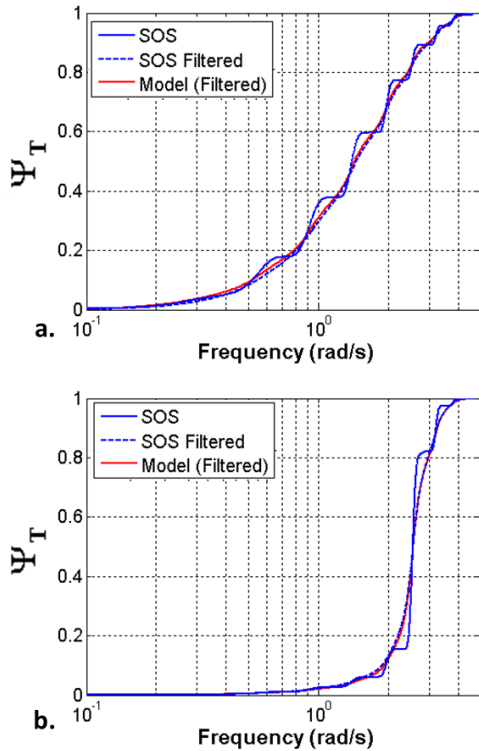


Figure 26.  $CSPR_T$  ( $\Psi_T$ ) model matching for SOS forcing spectra and ideal pilot: a)  $\omega_c=0.5$  rad/s,  $\tau=0.3$ s, phase margin=69 deg; b)  $\omega_c=2.5$  rad/s,  $\tau=0.5$ s, phase margin=12 deg.

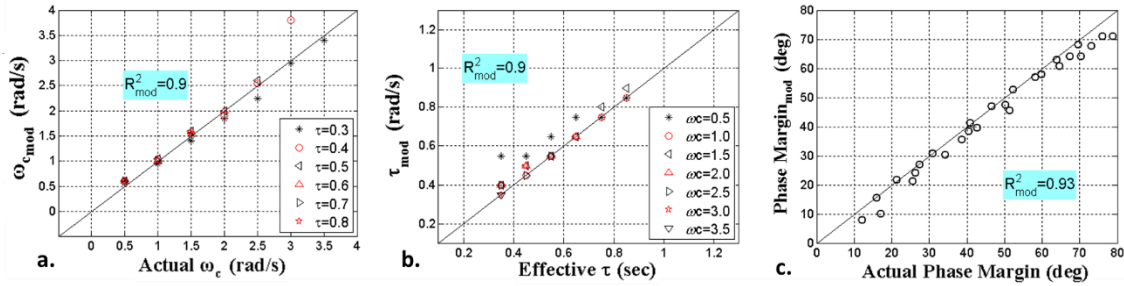


Figure 27. Parameter estimation by fitting  $\Psi_{T_{mod}}$  to  $\Psi_{T_{obs}}$  (sum-of-sines, acceleration command vehicle, simulated pilot lead  $\omega_{Ld} = 0.01$  and lag  $\omega_{Lg} = 20$  rad/s).

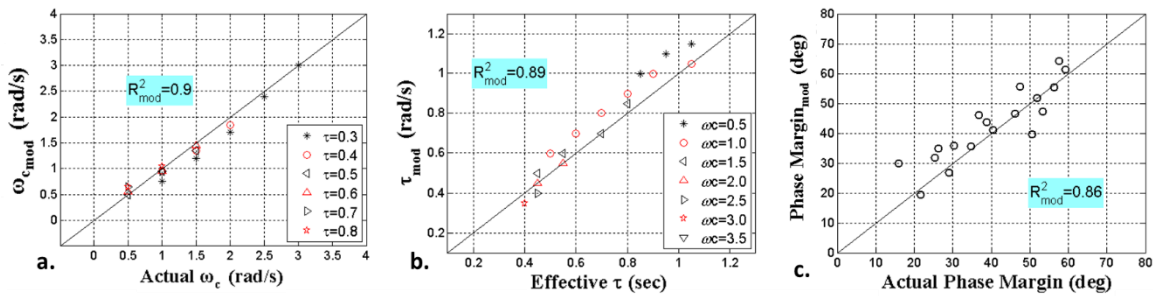


Figure 28. Parameter estimation by fitting  $\Psi_{T_{mod}}$  to  $\Psi_{T_{obs}}$  (sum-of-sines, acceleration command vehicle, simulated pilot lead  $\omega_{Ld} = 0.5$  and lag  $\omega_{Lg} = 5$  rad/s).

### 10. CSPR BOUNDING FREQUENCY

If the pilot behaved as a linear system, the spectral power of the stick response would reside only at the frequencies of the forcing function power. However, there are numerous sources of nonlinearities associated with the human operator which include broadband internal noise [Ref. 8], harmonics due to pulsing, and activation of the neuromuscular mode [Ref. 10]. Figure 29 shows two CSPR profiles for a pilot conducting the sum-of-sines tracking task used for this study. The profile on the right uses cumulative power out to 50 rad/s to normalize the power (CSPR), and the left profile uses 5 rad/s for bounding the CSPR computation. The highest frequency in the sum-of-sines forcing function was 4.7 rad/s, so that stick power beyond 5 rad/s should have been very low. Although there is a clear reduction in CSPR slope immediately following the last sum-of-sines frequency, power beyond 5 rad/s nonetheless comprised 40% of the total power!

The ratio of power above 5 rad/s to total power for all 81 runs conducted in the experiment is shown in Figure 30, the average ratio being 0.38. The effect of including the nonlinear high-frequency response is to skew the CSPR to the right (Figure 29). For

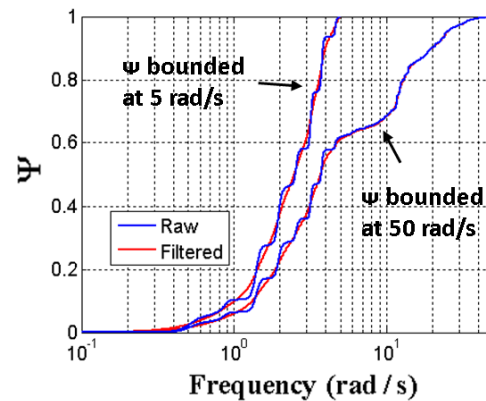
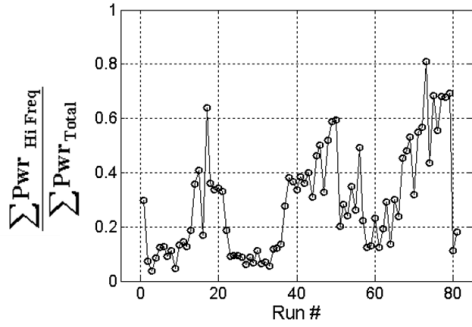


Figure 29. Comparison of frequency bounding effect on CSPR ( $\psi$ ).

this forcing function, terminating CSPR at the last SOS frequency is the obvious choice. For stochastic forcing functions such as gust, the bounding frequency should be sufficiently greater than the highest anticipated  $\omega_c$  such that when using the modeled CSPR<sub>τ</sub> (i.e., stick response is linear) Eq. 23 is satisfied.

$$(23) \quad \left[ \frac{\omega \psi_T^{bounded}}{\omega \psi_T^{unbounded}} \right]_{mod} \approx constant$$



**Figure 30. Ratio of power residing at frequencies greater than the forcing function bandwidth-to-total power (sum-of-sines task).**

This will allow a fixed  $\text{CSPR}_T$  to be used as a cutoff value (based on forcing function type). Absent nonlinear stick response, the bounding frequency skews  $\text{CSPR}_T$  to the left (i.e. the estimate for  $\omega_c$  is lower than actual), but the constant of Eq. 17 can be computed with the  $\text{CSPR}$  model and used to correct  $\omega_{\Psi_T}^{\text{bounded}}$ . Assuming  $\omega_c$  will be no greater than 5 rad/s [Ref. <sup>15</sup>], a bounding frequency of approximately 7 rad/s satisfies Eq. 17 for most time delays, while ensuring the proportion of high frequency stick power unrelated to the forcing function stays low.

Figure 31 shows the  $\text{CSPR}_T$  response (gust forcing function) for two different crossover frequencies when bounded at 7 rad/s compared to bounding at 50 rad/s (i.e., effectively unbounded). For any value of  $\text{CSPR}_T$  between approximately 0.1 and 0.8 the ratio in Eq. 23 is roughly constant as  $\omega_c$  is varied. For example, along the green line  $\Psi_T = 0.6$ , the ratio of bounded to unbounded frequency corresponding to  $\omega_c = 1$  rad/s is approximately the same as the ratio for  $\omega_c = 3$  rad/s.

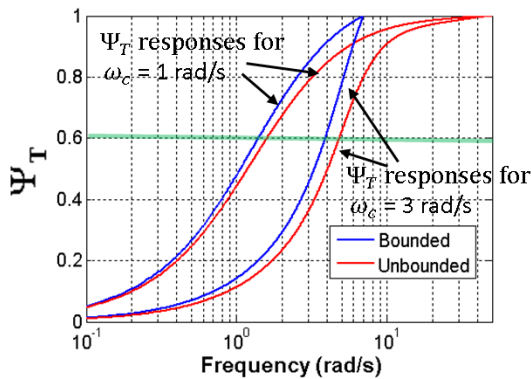


**Figure 31. Effect of bounding at 7 rad/s for two different crossover frequencies ( $\tau_{\text{eff}} = 0.2$  s, gust forcing function).**

If  $\text{CSPR}$  model matching is employed rather than a fixed  $\text{CSPR}$  value, the bounding frequency is

applied to both the observed and modeled  $\text{CSPR}_T$  so that no correction is needed.

## 11. ESTIMATING EFFECTIVE TIME DELAY USING $\text{CSPR}_T$ SLOPE

It was hypothesized previously a single cutoff value for  $\text{CSPR}_T$  can produce a reasonable estimate for  $\omega_c$  if the correct forcing function is accounted for in the estimate. A similar approach is sought for estimating the effective time delay using the same  $\text{CSPR}_T$  cutoff value as for  $\omega_c$ . For values greater than 0.2 sec,  $\tau_{\text{eff}}$  does not shift the location of the  $\text{CSPR}_T$  very much in frequency -  $\omega_c$  is the primary influence on  $\text{CSPR}_T$  shift. However, it was observed that  $\tau_{\text{eff}}$  can have a powerful influence on the slope of  $\text{CSPR}_T$  notably in the region of  $\omega_c$ . It was thus explored if slope at a single frequency contained reliable and sufficient information to obtain an estimate of  $\tau_{\text{eff}}$ . Eq. 22 (the definition of the modeled  $\text{CSPR}_T$ ) is repeated below

$$(22) \quad \Psi_T^{\omega} \text{ mod} = \frac{\frac{1}{2\pi} \int_0^{\omega} \frac{\omega_c^2 \omega^2}{(\omega^2 + \omega_c^2 - 2\omega\omega_c \sin\omega\tau)} S_{dd} d\omega}{\frac{1}{2\pi} \int_0^{\omega_B} \frac{\omega_c^2 \omega^2}{(\omega^2 + \omega_c^2 - 2\omega\omega_c \sin\omega\tau)} S_{dd} d\omega}$$

As the derivative of an integral is simply the integrand, the  $\text{CSPR}_T$  slope at frequency  $\omega$  is

$$(24) \quad \frac{d\Psi_T^{\omega}}{d\omega} \text{ mod} = \frac{\frac{1}{2\pi} \frac{\omega_c^2 \omega^2}{(\omega^2 + \omega_c^2 - 2\omega\omega_c \sin\omega\tau)} S_{dd}(\omega)}{\frac{1}{2\pi} \int_0^{\omega_B} \frac{\omega_c^2 \omega^2}{(\omega^2 + \omega_c^2 - 2\omega\omega_c \sin\omega\tau)} S_{dd} d\omega}$$

where  $S_{dd}(\omega)$  is the forcing function at frequency  $\omega$ . The term  $\sin\omega\tau$  prevents the integral in the denominator from being evaluated analytically. A convenient simplification is to assume  $\omega\tau \ll 1$  so that  $\sin\omega\tau \approx \omega\tau$ , however, it is seen in the experimental results that  $\omega\tau$  can often approach and even exceed unity. Evaluating Eq. 24 at  $\omega = \omega_c$  yields

$$(25) \quad \frac{d\Psi_T^{\omega_c}}{d\omega} = \frac{\omega_c^2 S_{dd}(\omega_c)}{2\omega_c(1 - \sin\omega_c\tau) \int_0^{\omega_B} \frac{\omega_c^2 \omega^2}{(\omega^2 + \omega_c^2 - 2\omega\omega_c \sin\omega\tau)} S_{dd} d\omega}$$

When the forcing function  $S_{dd}$  is discrete (i.e., SOS),  $\Psi_T^{\text{mod}}$  is also discrete. Since the  $\text{CSPR}_T$  slope associated with using the discrete SOS is not useful (it is either zero or infinity), the discrete parent spectrum is extended to the continuous domain and used in its stead. The parent SOS forcing function employed in the workload experiment was

$$(26) \quad S_{dd}(\omega_i) = \frac{2\pi}{d\omega} \sum_{i=1}^N \frac{A_i^2}{2}, \quad A_i = \log_{10} \left( \frac{\beta}{\omega_i} \right)$$

where  $\beta$  is a constant. The continuous analogue is given by Eq. 27

$$(27) \quad S_{dd}(\omega) = \left[ \log_{10} \left( \frac{\beta}{\omega} \right) \right]^2$$

Applying the spatial filter to the transformed stick  $\delta_T$  produces a continuous  $\Psi_T^f$  (Figure 25), which alters the relationship in Eq. 24. This alteration was not relevant with model-matching since the same filtering was applied to both the observed stick signal and the discrete CSPR<sub>T</sub> model. In this case, however, it needs to be established whether the CSPR<sub>T</sub> slope produced by the continuous forcing function spectrum is well-represented by the filtered CSPR<sub>T</sub>. Figure 32 shows that the CSPR<sub>T</sub> slopes produced by the spatially-filtered discrete SOS and the continuous SOS analogue match well, and this was observed for most combinations of  $\omega_c$  and  $\tau$  within the range of phase margins  $0 < PM < 80$  degrees. We now have the confidence to use the spatial filter response to generate  $\frac{d\Psi}{d\omega}$  in Eq. 24.

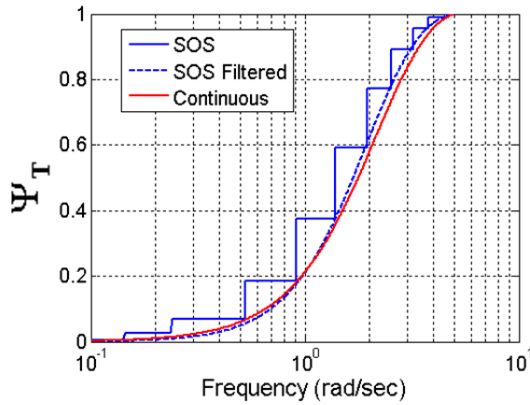


**Figure 32. Comparison of CSPR<sub>T</sub> generated from different spectra sources: discrete SOS, filtered SOS, and continuous parent of SOS ( $\omega_c=1.0$  rad/s,  $\tau=0.3$ s, phase margin=69 deg).**

Eq. 25 contains the ratio

$$(28) \quad \frac{S_{dd}(\omega_c)}{\int_0^{\omega_B} \frac{\omega_c^2 \omega^2}{(\omega^2 + \omega_c^2 - 2\omega\omega_c \sin\omega\tau)} S_{dd} d\omega} = \frac{[\log_{10}(\frac{\beta}{\omega_c})]^2}{\int_0^{\omega_B} \frac{\omega_c^2 \omega^2}{(\omega^2 + \omega_c^2 - 2\omega\omega_c \sin\omega\tau)} [\log_{10}(\frac{\beta}{\omega})]^2 d\omega}$$

which cannot be analytically evaluated. Using  $\omega_B = 5$  rad/s (SOS bandwidth) and iterating over  $\omega$  and  $\tau$ , it was observed that Eq. 28 is approximately proportional to the inverse of the crossover frequency squared, i.e.,

$$(29) \quad \frac{[\log_{10}(\frac{\beta}{\omega_c})]^2}{\int_0^{\omega_B} \frac{\omega_c^2 \omega^2}{(\omega^2 + \omega_c^2 - 2\omega\omega_c \sin\omega\tau)} [\log_{10}(\frac{\beta}{\omega})]^2 d\omega} \propto \frac{1}{\omega_c^2}$$

Eq. 25 can then be rewritten as

$$(30) \quad \frac{d\Psi_T^{\omega_c}}{d\omega} \approx \frac{K}{(1 - \sin\omega_c\tau)}$$

We can now isolate  $\tau$  in Eq. 31,

$$(31) \quad \tau = \frac{1}{\omega_c} \sin^{-1} \left( 1 - \frac{K}{\frac{d\Psi_T^{\omega_c}}{d\omega}} \right)$$

Iterating over a broad range of values for  $\tau$  and  $\omega_c$  in the CSPR<sub>T</sub> model (the phase margin was maintained within  $0 < PM < 80$  degrees), a best match between estimated and simulated  $\tau$  was obtained using a value of  $K = 0.35$  in Eq.31. Both  $\omega_c$  and  $\frac{d\Psi}{d\omega}$  in Eq. 31 used the frequency and slope associated with  $\Psi_T = 0.4$  (an approximate average of the CSPR<sub>T</sub> response from Figure 19b). This produced the  $\tau$  estimates shown in Figure 33 ( $R_{mod}^2 = 0.92$ ). It is remarkable how the apparently complex relationship in Eq. 24 reduced to the elementary form of Eq. 30, and that this yielded quite precise estimates of  $\tau_{eff}$ . As will be seen in the experimental results section, employing Eq. 31 with no modification likewise generated good estimates of  $\tau_{eff}$ .

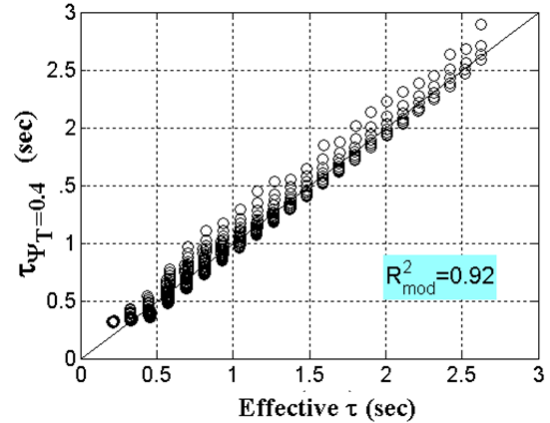


**Figure 33. Time delay estimate employing CSPR<sub>T</sub> slope and frequency at CSPR<sub>T</sub> cutoff = 0.4 using a broad range of  $\tau$  and  $\omega_c$  values in the CSPR<sub>T</sub> model (SOS forcing function).**

When computing  $\tau$  using the transformed cutoff method, the frequency used to estimate  $\omega_c$  is the frequency corresponding to the cutoff value appropriate for the forcing function. A SOS spectrum different from the one used here will produce a CSPR<sub>T</sub> response different from Figure 19b (Figure 19b is equivalent to the CSPR<sub>T</sub> response). The CSPR<sub>T</sub> model (Eq. 22) would be used to compute the family of responses due to varying  $\tau_{eff}$ , from which the cutoff value would be obtained.

## 12. CUMULATIVE OUTPUT POWER RATIO: EMPLOYING VEHICLE OUTPUT TO ESTIMATE SYSTEM BANDWIDTH

Repeating the stick transformation relation given by Eq. 18,

$$(18) \quad \delta_T(s) = \delta(s)Y_v(s)s$$

it can be seen that  $\delta(s)Y_v(s)$  is simply the vehicle output  $y(s)$  (Figure 3). It is equivalent to write

$$(32) \quad \delta_T(s) = y(s)s$$

which is the differentiated vehicle output. Thus, replacing the transformed stick  $\delta_T$  in  $CSPR_T$  with the differentiated vehicle output produces the same result. A significant difference in practice is that  $\delta_T$  requires an assumption or measurement of the vehicle dynamics  $Y_v$ , whereas employing the output avoids this potentially complex and imprecise procedure.

Using the raw vehicle output  $y$  in a newly defined "cumulative output power ratio" (COPR) computation,

$$(33) \quad COPR_\omega = \frac{\frac{1}{2\pi} \int_0^\omega S_{yy} d\omega}{\frac{1}{2\pi} \int_0^\infty S_{yy} d\omega}$$

where

$$(34) \quad \frac{1}{2\pi} \int_0^\infty S_{yy} d\omega = \frac{1}{2\pi} \int_0^\infty |G_{dy}|^2 S_{dd} d\omega$$

$$(35) \quad G_{dy} = \frac{Y_D Y_P Y_V}{1 + Y_D Y_P Y_V} = \frac{\omega_c e^{-\tau s}}{(s + \omega_c e^{-\tau s})}$$

Eq. 35 has the same form as  $G_{d\delta_{prop}}$  in Eq. 16, which produced the CSPR response shown in Figure 17a (gust spectrum). This response rises to unity well before  $\omega_c$  providing no useable information about where  $\omega_c$  occurs. However,  $G_{d\delta_{rate}}$  in Eq. 16 (created by adding a free  $s$  in the numerator of  $G_{d\delta_{prop}}$ ) did produce a well-behaved CSPR response. Adding a free  $s$  to Eq. 35 will generate the same favorably shaped power ratio response. Effectively this transforms COPR, yielding

$$(36) \quad COPR_T^\omega = \frac{\frac{1}{2\pi} \int_0^\omega S_{y_T y_T} d\omega}{\frac{1}{2\pi} \int_0^\infty S_{y_T y_T} d\omega}$$

where

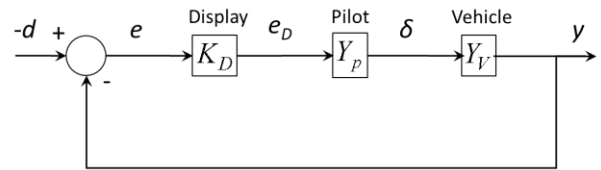
$$(37) \quad y_T(s) = y(s)s$$

If there is high confidence in the vehicle dynamics there may be situations when it would be preferable to employ  $CSPR_T$  over  $COPR_T$ , such as when a) there is considerable noise in the vehicle output due to sensing, and/or b) the vehicle output is unreliable or unavailable.

## 13. WORKLOAD EXPERIMENT

An experiment was conducted that investigated the relationship between vehicle input/output states and pilot workload. Four command vehicle dynamics (proportional, rate, acceleration, jerk), vehicle gains (vehicle sensitivity to input), and display gains (display sensitivity to error) were used with a lateral station-keeping using a compensatory display, where a random forcing function continuously disturbed ownship's position.

Figure 34 shows a representation of the station-keeping task and the display ( $K_D$ ), pilot ( $Y_P$ ) and vehicle ( $Y_V$ ) components of the closed-loop system, and the range of conditions within each component that were tested. The jerk condition for the vehicle dynamics (fourth condition listed for  $Y_V$ ), contains a pole  $p$  whose location was varied. Subjects were tested using various combinations of the conditions shown in Figure 34. The configurations were selected to maximally span the Bedford rating over all vehicle command dynamics. Since pilot proficiency with any test condition was not a factor in this experiment, pilots were given two practice runs with each vehicle dynamic type (proportional, rate, acceleration, jerk) prior to testing.



$$Y_V = \left\{ K_V, \frac{K_V}{s}, \frac{K_V}{s^2}, \frac{K_V}{(s+p)s^2} \right\}$$

$$K_V = \left\{ 5, 10, 30, 60 \right\} \quad p = \left\{ 1, 2, 5 \right\}$$

$$K_D = \left\{ 0.5, 2, 4, 8, 32 \right\}$$

$$Y_D Y_P Y_V(s) \Big|_{\omega_c} \approx \frac{\omega_c}{s} e^{-s\tau}$$

**Figure 34. Station-keeping task: Pilot, display, vehicle elements, and range of conditions for display and vehicle elements.**

One may be tempted to think that the display gain and the vehicle gain are effectively interchangeable and the same gains from the pilot's vantage point. The following example will serve to disprove this common misnomer. If the pilot's input is zero, the disturbance is perceived through the display gain – the vehicle gain does not come into play at all. Based on his/her control activity and quiescence, a pilot learns to decouple the effects of the display gain from the vehicle gain – thus decoupling aircraft motion due to disturbance from pilot-commanded vehicle motion.

Four male participants took part in the study. Three were Experimental Test Pilots (graduates of Navy

Test Pilot School) with 1,900, 1,900, and 2,450 rotary wing flight hours. The fourth participant had logged 800 hours of rotary wing flight time. Ownship error relative to the target location was displayed on a laptop monitor (Figure 35), and the pilot attempted to minimize the error using a gamepad joystick (Logitech Dual Action gamepad).

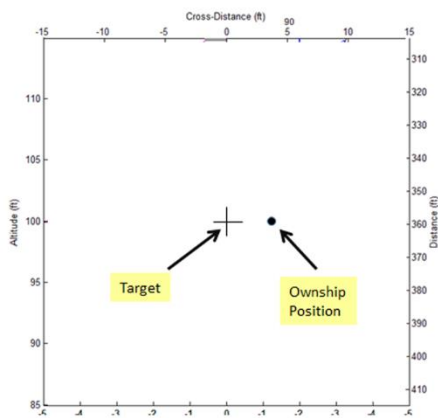


**Figure 35. Simulation environment: Gamepad, laptop, display showing target and ownship positions.**

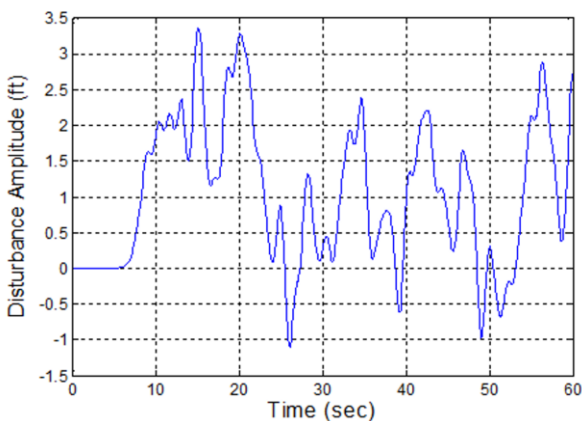


**Figure 36. Positional disturbance of ownship.**

The Bedford rating scale [Ref. 16] was used to subjectively score each pilot's spare capacity at the end of each 60-second tracking run. Dependent qualitative variables were: stick position, rate and acceleration, stick position reversals, display error, rate, and acceleration. The positional disturbances imposed on the helicopter were designed to be

both realistic and a diagnostic probe for pilot control behavior. Composed of a sum of 11 non-harmonically-related sine waves, the disturbance was perceived by the pilot as a random process – the result, however, was that the pilot's control response power resided largely at the same frequencies contained in the input disturbances. The disturbance time history is shown in Figure 36 (it ranged from approximately -1 to 3 feet, with a standard deviation of 1 foot). The experiment's Bedford rating and estimation results are given in [Ref. 17].

## 14. RESULTS

### 14.1. Equivalent Crossover Model System Identification

The effective time delays computed using the Crossover Model as the lower order equivalent system (LOES, Figure 8) for all conditions and pilots are shown in Figure 37. These time delays

result from both pilot processing delay (Figure 5) and the pilot's departure from compensating for vehicle dynamics according to the idealized Crossover Model. The vertical axis is vehicle type (proportional, rate, acceleration, and jerk command). There is a very strong clustering effect of vehicle type on effective time delay, with virtually no overlap between types.

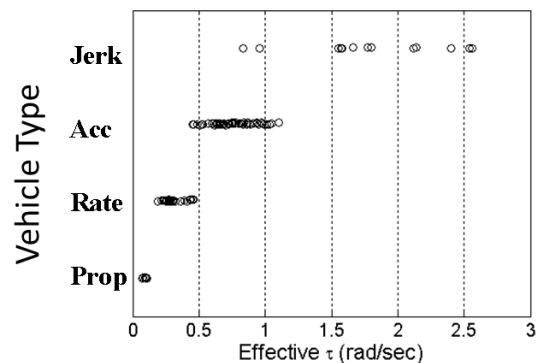


**Figure 37. Effective time delay by vehicle type.**

Figure 38 sorts effective crossover frequency by vehicle type. There is no clear trend except that  $\omega_{c_{eff}}$  appears to lowest for the jerk dynamics. Eq. 4 was used to compute the effective phase margins from  $\omega_{c_{eff}}$  and  $\tau_{T_{eff}}$ , shown in Figure 39. While not as strongly influenced by type as  $\tau_{T_{eff}}$ , effective phase margin monotonically decreases going from proportional to jerk command dynamics. Note that the experimental conditions varied the vehicle dynamics, control gain and display gain. These three factors each contributed to perceived task

difficulty [Ref. 18], yet it appears that vehicle type was the dominant influence on  $\tau_{Teff}$  and effective phase margin. Correlation between Bedford ratings and both  $\tau_{Teff}$  and effective phase margin was poor, further reinforcing the observation that task difficulty and stability margin is loosely coupled.

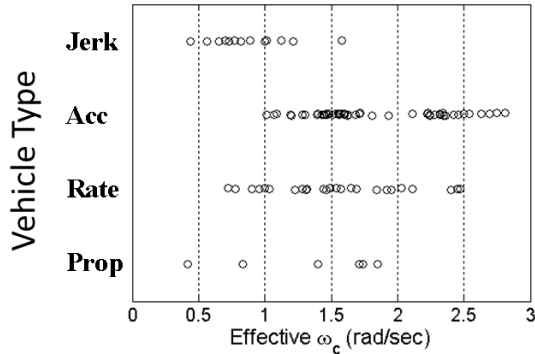


Figure 38. Effective crossover by vehicle type.

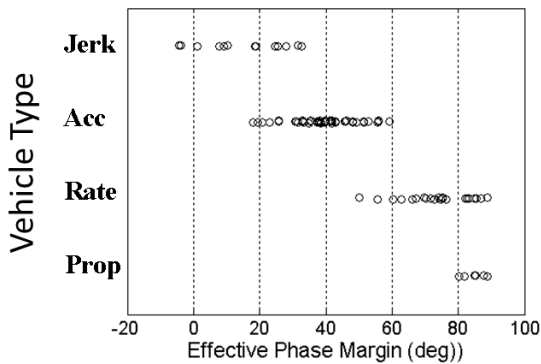


Figure 39. Effective phase margin by vehicle type.

The open-loop frequency response for a pilot flying jerk-command dynamics is given in Figure 40a. The magnitude ratio undulates above and below 0 dB for part of the response, and is an excellent example of how much pilot compensation can deviate from the Crossover Model's ideal -20 dB/decade slope (i.e., an integrator) at crossover. In fact, this example demonstrates a case where crossover is difficult to visually or otherwise identify. Fitting the equivalent Crossover system to the observed time response of the output produces a fair match in Figure 40b, yielding  $\omega_{ceff} = 1.3$  rad/s and  $\tau_{eff} = 0.8$  sec.

In order to compare  $\omega_c$  obtained from the open-loop frequency response with  $\omega_{ceff}$ , the frequency response-computed  $\omega_c$  was defined as the highest interpolated frequency where the magnitude ratio was within a minimum distance from 0 dB. The two are compared (using all 81 runs with mixed vehicle

types) in Figure 41, and as hoped the correspondence between the two is good.

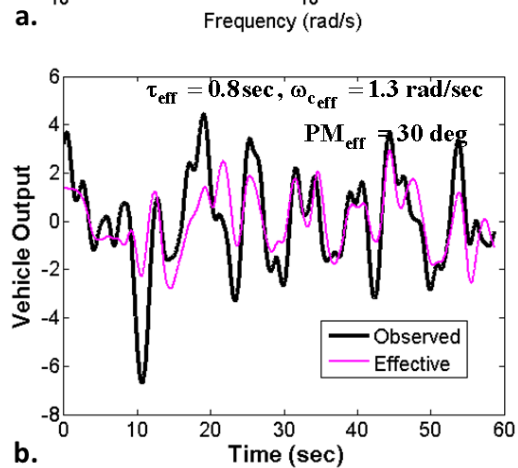
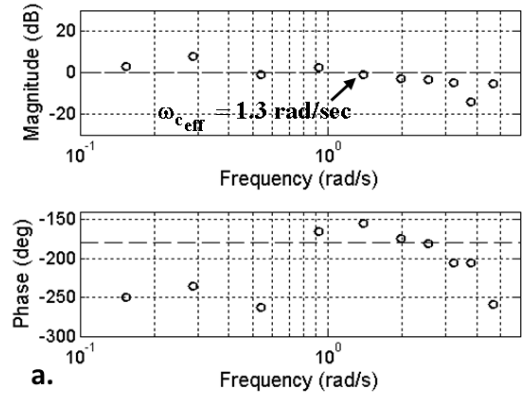


Figure 40. a) Open-loop frequency response for jerk command vehicle; b) Equivalent crossover system output for jerk command vehicle and observed system output.

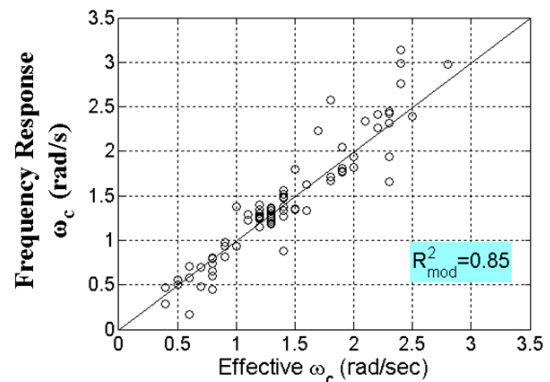


Figure 41. Comparison of effective crossover frequency with crossover frequency computed from the frequency response for all runs (N=81).

## 14.2. Pilot Cutoff Frequency Analysis and Conditioning

Figure 42 applies the original pilot cutoff frequency ( $\omega_{co}$ ) criterion of CSPR = 0.5 to the raw stick data

using three conditions (note this power ratio does not use the stick transformation). In Figure 42a there is neither spatial filtering nor CSPR bounding, and in general  $\omega_{co}$  greatly exceeds  $\omega_{ceff}$ . In Figure 42b spatial filtering is applied and CSPR while still unbounded, which improves the estimate. In Figure 42c both spatial filtering and CSPR bounding at 5 rad/s are employed. Looking at the CSPR responses for the SOS forcing function in Figure 19, one sees that a CSPR value of 0.5 produces estimates that are generally high for the rate command dynamics, and very high for acceleration command dynamics. Estimation of  $\omega_c$  using  $\omega_{co}$  with proportional command dynamics would tend to be better at moderate values of crossover, but these dynamics comprise only 8% of the total. Figure 42c demonstrates the utility of spatial filtering and bounding when computing  $\omega_{co}$  even when the tracked state is not consistent with the originally intended dynamics (i.e. rate-commanded).

Figure 43b compares  $\omega_{co}$  with  $\omega_{ceff}$  when the vehicle type is consistent with the definition of  $\omega_{co}$ , and there is an improvement compared to Figure 43a where all types were used. Once again, Figure 19b predicts overshoot for rate command dynamics for CSPR = 0.5.

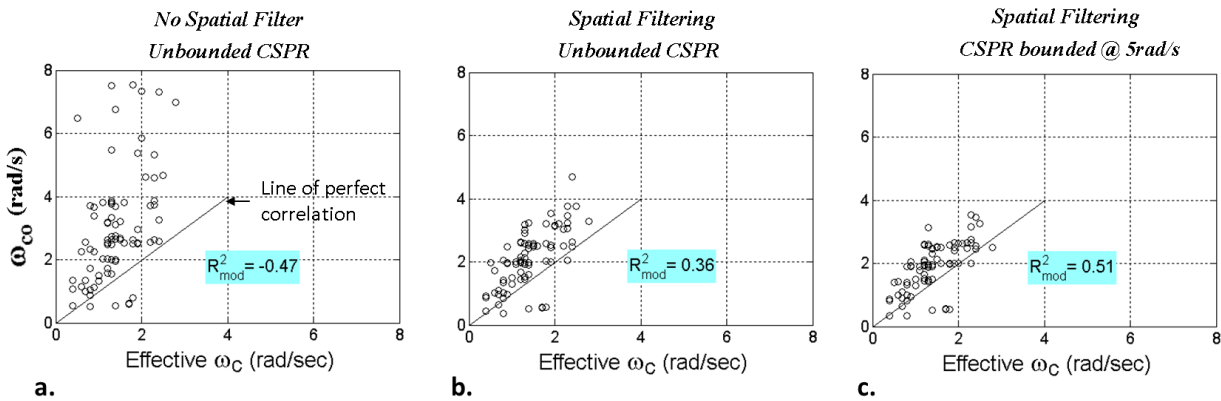


Figure 42. Pilot Cutoff Frequency (all vehicle types, stick transformation not employed): a) No spatial filtering and unbounded CSPR; b) Spatial filtering and unbounded CSPR; c) Spatial filtering and CSPR bounded at 5 rad/s.

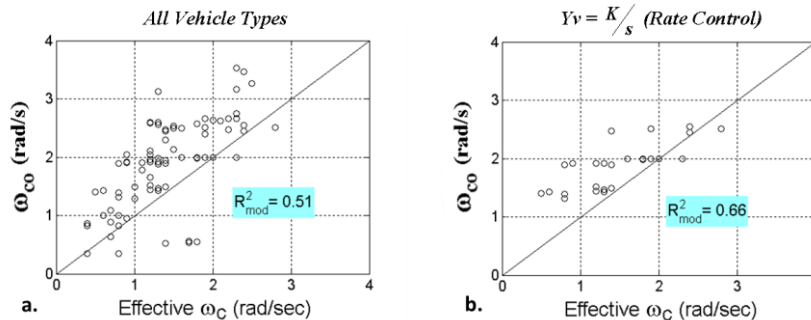


Figure 43. Pilot Cutoff Frequency (spatial filtering and CSPR bounding employed): a) All vehicle types; b) Rate command dynamics.

### 14.3. Transformed CSPR (CSPR<sub>T</sub>) Analysis

Using 0.5 as the cutoff value for CSPR<sub>T</sub> (which employs the transformed stick using Eq. 18, spatial filtering, and CSPR<sub>T</sub> bounding), correlation between estimated and effective crossover for all vehicle types increases from 0.51 to 0.69, shown in Figure 44. All CSPR<sub>T</sub>-related analysis from here onward employs spatial filtering and CSPR bounding.

Figure 45 plots each value of CSPR<sub>T</sub> corresponding to  $\omega_{ceff}$  for all 81 runs. Figure 19b shows the range of CSPR<sub>T</sub> response when  $\tau_{eff}$  is varied, and this is generally reflected in the variation of CSPR<sub>T</sub> in Figure 45. The CSPR<sub>T</sub> responses in Figure 19b were limited to effective phase margins greater than 10 degrees, however, the experiment exhibited effective phase margins that were even negative in value, which would account for the CSPR<sub>T</sub> values near or below 0.2 in Figure 45. The mean CSPR<sub>T</sub> for all runs in Figure 45 is 0.4, which again could be estimated looking at Figure 19b. This mean CSPR<sub>T</sub> value is used in Figure 46, producing a high correlation with  $\omega_{ceff}$  ( $R^2_{mod} = 0.83$ ).

$\tau_{eff}$  was estimated using Eq. 31, with the slope of  $CSPR_{\tau}$  evaluated at  $\Psi_{\tau} = 0.4$  (looking at Figure 45 a cutoff value of 0.4 closely corresponds to  $\omega_{ceff}$ ).

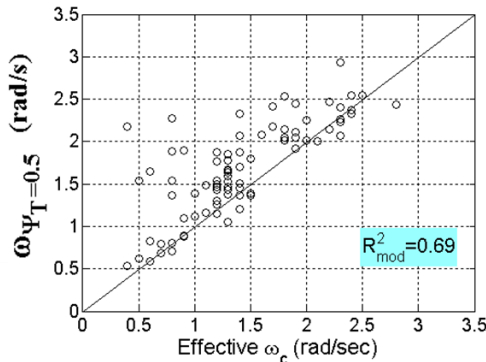


Figure 44.  $CSPR_{\tau}$  frequency associated with  $\psi_{\tau} = 0.5$  (all vehicle types).

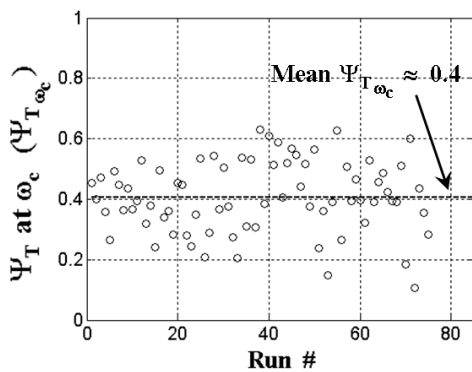


Figure 45.  $CSPR_{\tau}$  ( $\Psi_{\tau}$ ) corresponding to effective  $\omega_c$ .

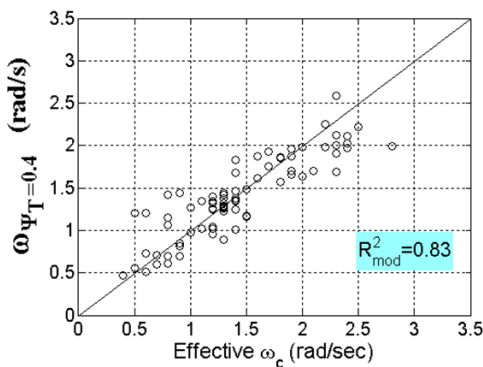


Figure 46.  $CSPR_{\tau}$  frequency associated with  $\psi_{\tau} = 0.4$  (all vehicle types).

Figure 47 compares  $\tau_{eff}$  with the time delay estimated using the slope and frequency at  $\psi_{\tau} = 0.4$  (Eq. 31). Note this is not  $R^2_{mod}$  (Eq. 5) since the goodness-of-fit here is relative to the best-fit line between the estimate and  $\tau_{eff}$ .

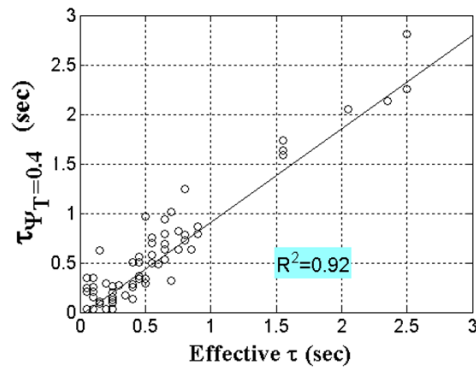


Figure 47. Best-fit between estimated and actual effective time delay (estimate computed using Eq. 27).

Figure 48 shows side by side the estimates for  $\omega_{ceff}$  and  $\tau_{eff}$  (using the cutoff  $\psi_{\tau} = 0.4$ ) with the actual values. The estimated  $\tau$  was computed using the best-fit line from Figure 47, with the  $R^2_{mod}$  reflecting the error between the estimate and actual. It is noteworthy that a single cutoff value for  $CSPR_{\tau}$  produces robust estimates of  $\omega_{ceff}$  and  $\tau_{eff}$  despite such wide-ranging  $\tau_{eff}$ . It should be remembered that the workload experiment also included jerk-command vehicle dynamics. The stick transformation effectively normalized all dynamics so that the  $CSPR_{\tau}$  response was identical for all of them, allowing  $CSPR_{\tau}$  frequency and slope to be used irrespective of vehicle type.

#### 14.4. $CSPR_{\tau}$ -Crossover Model Matching

The estimates for for  $\omega_{ceff}$  and  $\tau_{eff}$  using  $CSPR_{\tau}$ -Crossover Model matching are shown in Figure 49. The correlation between estimate and actual is good, but less than when using the transformed cutoff  $\psi_{\tau} = 0.4$ . Figure 50 compares the effective phase margin estimates using the cutoff approach ( $\psi_{\tau} = 0.4$ ) and the  $CSPR_{\tau}$ -Crossover Model matching method. Although the individual correlations for  $\omega_{ceff}$  and  $\tau_{eff}$  were higher using the transformed cutoff method, the product of the two parameters (employed in the phase margin computation) resulted better correlation using  $CSPR_{\tau}$ -Crossover Model matching. Thus the former technique may be preferable for bandwidth estimation, and the latter for stability margin estimation.

The same investigation and analysis was conducted using the transformed cumulative output power ratio (COPR $_{\tau}$ ) technique, producing near-identical results. This is to be expected since mathematically both COPR $_{\tau}$  and  $CSPR_{\tau}$  are equivalent and the vehicle dynamics used in the experiment were precisely known.

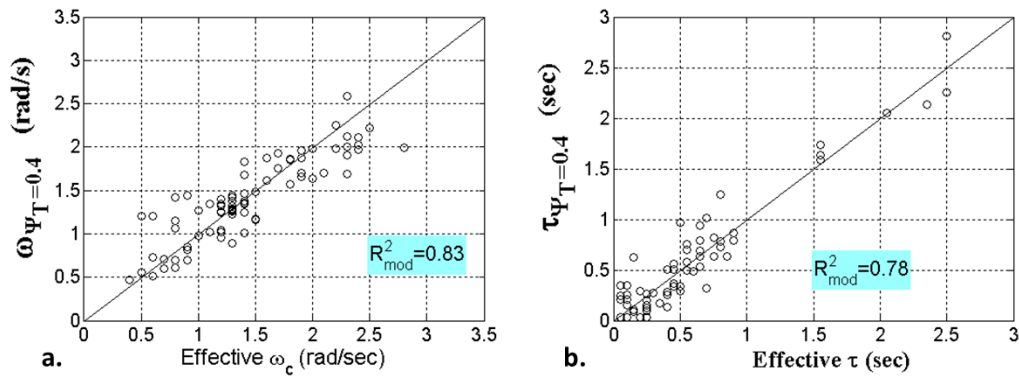


Figure 48. Comparison of estimates for  $\omega_{c_{eff}}$  and  $\tau_{eff}$  associated with  $\psi_T = 0.4$ .

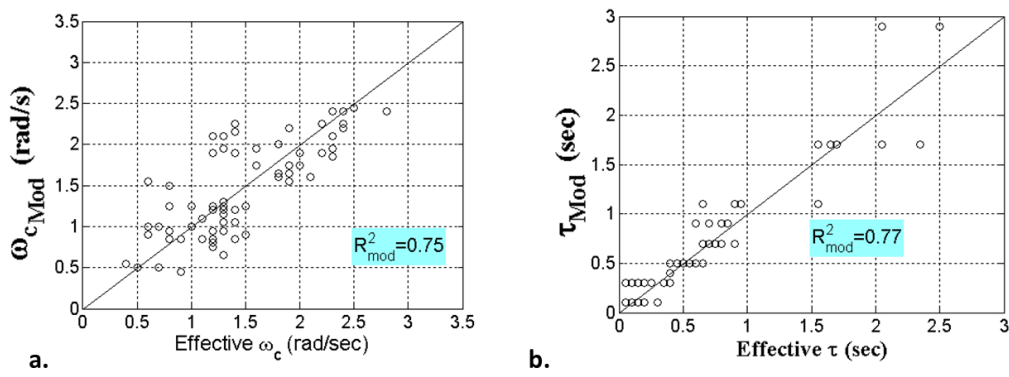


Figure 49. Comparison of estimates for  $\omega_{c_{eff}}$  and  $\tau_{eff}$  using C\_SPT-Crossover Model matching.

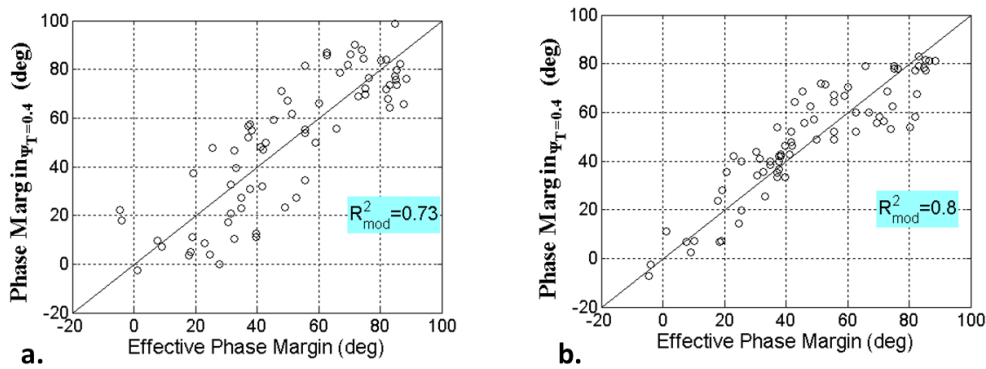


Figure 50. Comparison of estimated to actual effective phase margin using: a) cutoff  $\psi_T = 0.4$ ; b) C\_SPT-Crossover Model matching.

## 15. SUMMARY AND CONCLUSIONS

### 15.1. Estimation Techniques

A standard metric to estimate system bandwidth is the pilot cutoff frequency, which is the frequency at which the cumulative power ratio of the pilot's

control response equals 0.5. Implicit with using the pilot cutoff frequency is that the vehicle output being tracked is approximately the integral of the control input (i.e., rate-commanded). However, errors in estimation will occur when the technique is applied to systems whose tracked outputs differ significantly from this assumption. Furthermore, the type of disturbance spectrum impinging on the

tracking task has a strong influence. The effect of these factors on pilot cutoff frequency was examined theoretically, and a method for transforming the cumulative control power ratio was developed that enables the transformed ratio to be applied to any tracked state. A method for determining effective time delay, and effective phase and gain margin from the slope of the transformed cumulative power ratio was also developed.

Assuming knowledge of the disturbance spectrum and vehicle dynamics, two techniques were offered to estimate system bandwidth and time delay using: 1) A cutoff frequency (dependent on the forcing function) using the transformed stick response cumulative power ratio; 2) Iteration on the crossover frequency and time delay parameters in the closed-loop Crossover Model until a best match is found between the transformed cumulative power ratios of the modeled and observed stick response. The latter approach does not require that the forcing function contain power extending to or beyond crossover. The development demonstrates that bounding the upper frequency of the computed control power is a critical step of the estimation process, as this reduces the effect of uncorrelated high frequency content arising from sources such as the neuromuscular mode and harmonics of pulse-like control on the estimates. A unique bi-directional spatial filter that allows the frequency and slope from cumulative power ratios to be continuously analyzed when using discrete spectra forcing functions (such as sum-of-sines) was also developed. The filter improves estimation when the forcing spectrum is continuous.

A new system bandwidth estimation method that uses the vehicle output cumulative power ratio was proposed, which unlike the cumulative stick power approach does not require an assumption about or measurement of the vehicle dynamics. This technique transforms the output by simple differentiation, allowing similar application of the stick power methods (cumulative power ratio cutoff and model matching).

Finally, effective time delay and crossover frequency are estimated using the ideal Crossover Model by matching the observed system time response. The novelty introduced here is that the effective stability margin arising from these two effective parameters closely coincides with the actual system stability margins (phase and gain), irrespective of the differences between the idealized and actual dynamics. This allows the accuracy of any bandwidth estimate to be assessed – establishing the actual bandwidth associated with human-in-loop operation has

heretofore proven elusive. The technique lends itself to both manual and automated systems and will be useful for assessing handling qualities.

## 15.2. Experimental Results

Actual pilot data obtained from a simulation tracking experiment demonstrated the efficacy of these various estimation techniques.  $\omega_{c_{eff}}$  estimation was superior using the transformed cutoff method, whereas estimates of effective phase margin were generally better using CSPR<sub>T</sub>-Crossover Model matching. Both approaches produced similarly good estimates of  $\tau_{c_{eff}}$ . An important advantage of Crossover Model matching is that unlike the cutoff approach it does not require that the operator's stick response contain power in the region of crossover – an estimate can be generated even when the stick response power is primarily low frequency.

Vehicle type had a strong influence on effective time delay, with virtually no overlap between types. A similar effect was observed with effective phase margin. Note that the experimental conditions varied the vehicle dynamics, control gain and display gain. These three factors each contributed to perceived task difficulty, yet it appears that vehicle type was the dominant influence on  $\tau_{eff}$  and effective phase margin.

## 15.3. Future Work

A mathematical basis for the phase margin agreement between an actual system and its Crossover Model equivalent will be presented in future work together with its application to aircraft handling qualities.

## 16. NOMENCLATURE

<i>CSPR</i>	Cumulative stick power ratio
<i>COPR</i>	Cumulative output power ratio
<i>LOES</i>	Low order equivalent system
<i>CIFER</i>	Comprehensive Identification from Frequency Response software package
<i>PSD</i>	Power spectral density
<i>SOS</i>	Sum-of-sines
<i>dB</i>	Decibels, $20\log_{10}()$
$d(t)$	Forcing function signal
$e(t)$	Error signal
$e$	Euler's number, base of the natural logarithm
<i>GM</i>	Gain margin
<i>PM</i>	Phase margin
$\ln$	Natural logarithm
$\log_{10}$	Logarithm base 10
$R^2$	Correlation coefficient
$R^2_{mod}$	Modified correlation coefficient

$Y_{xy}$	Transfer function, x output y input
$Y_D$	Display transfer function
$Y_p$	Pilot describing function
$Y_v$	Vehicle transfer function
$s$	Complex variable, Laplace transform variable
$t$	Time (sec)
$S_{dd}$	Forcing function power spectral density
$S_{\delta\delta}$	Stick power spectral density
$\delta(t)$	Stick signal
$\delta_T$	Transformed stick signal
$\Psi$	Cumulative stick power ratio
$\Psi^f$	Spatially filtered $\Psi$
$\Psi_T$	Transformed cumulative stick power ratio
$\sigma_\delta^2$	Variance (power) of signal $\delta(t)$
$\tau_{eff}$	Effective time delay
$\omega$	Angular frequency, rad/s
$\omega_B$	Bounding frequency
$\omega_c$	System crossover frequency
$\omega_{co}$	Pilot cutoff frequency
$\omega_{gc}$	Gain crossover frequency (also $\omega_c$ )
$\omega_{pc}$	Phase crossover frequency
$\omega_{c_{eff}}$	Effective crossover frequency
$\omega_{hp}$	Half-power frequency

## 17. ACKNOWLEDGMENTS

Mark Tischler provided key information related to the development and background of his pilot cutoff metric, and Bob Heffley offered invaluable insight on nested loop operation. This work was supported by cooperative agreement NNX16AJ91A between the U.S. Army Aviation Development Directorate and San Jose State University. This paper is dedicated to the memory of Duane McRuer.

## 1. REFERENCES

- Tischler, M. B., & Remple, R. K. (2006). Aircraft and rotorcraft system identification. AIAA education series, 72.
- Biernson, G. A. (1988). Principles of feedback control. John Wiley & Sons, Inc.
- Atencio Jr, A. (1993). Fidelity assessment of a UH-60A simulation on the nasa ames vertical motion simulator.
- Lampton, A., & Klyde, D. (2012). Power Frequency: A metric for analyzing pilot-in-the-loop flying tasks. *Journal of Guidance, Control, and Dynamics*, 35(5), 1526-1537.
- Moré, A. G. (2014). A Quantitative Evaluation of Pilot-in-the-Loop Flying Tasks Using Power Frequency and NASA TLX Workload Assessment.
- Tritschler, J. K., & O'Connor, J. C. (2016). Use of Time-Frequency Representations for Interpreting Handling Qualities Flight Test Data. *AIAA Journal*, 2772-2779.

## 18. BIOGRAPHIES

Dr. Edward Bachelder is a senior Research Engineer at ADD, Moffett Field, CA. Dr. Bachelder received his MS in Aircraft Dynamics and Control from Purdue University in 1987, after which he entered Navy pilot training and flew the SH-60B Seahawk helicopter. Following active duty in 1994 he entered MIT's School of Aeronautics and Astronautics doctoral program, receiving his PhD in 2000 from the Division of Humans and Automation. Subsequent to a post-doctorate with Nancy Leveson's Software Engineering Research Lab at MIT investigating operator mode confusion, he worked from 2001 to 2015 at Systems Technology Inc. (STI) as Principal Research Engineer and Technical Director of Fused Reality, a Mixed Reality technique he coined, patented and developed. His current research includes modelling pilot control and workload, and advanced display design.

Mr. Bimal Aponso is the Chief of the Aeronautics Projects Office at NASA Ames Research Center. Bimal's technical background includes over 25-years of experience in vehicle modeling and simulation, stability and control, and handling qualities, both in government and in Industry. He researched, designed and developed flight control systems for several military and civil aircraft and rotorcraft, and contributed to several Military Specifications on aircraft/rotorcraft handling qualities.

<sup>7</sup> Fujizawa, B. T., Lusardi, J. A., Tischler, M. B., Braddom, S. R., & Jeram, G. J. (2011, May). Response Type Tradeoffs in Helicopter Handling Qualities for the GVE. In American Helicopter Society 67th Annual Forum, Virginia Beach, VA.

<sup>8</sup> McRuer, D. T. and Krendel, E. S. (1974). *Mathematical Models of Human Pilot Behavior*, (No. AGARD-AG-188). ADVISORY GROUP FOR AEROSPACE RESEARCH AND DEVELOPMENT NEUILLY-SUR-SEINE (FRANCE).

<sup>9</sup> Hess, R. A., "Unified Theory for Aircraft Handling Qualities and Adverse Aircraft-Pilot Coupling", *Journal of Guidance, Control, and Dynamics*, Vol. 20, No. 6, 1997.

<sup>10</sup> Bachelder, Edward N., Ronald A. Hess, Martine Godfroy-Cooper, and Bimal L. Aponso. "Linking the Pilot Structural Model and Pilot Workload." In *2018 AIAA Atmospheric Flight Mechanics Conference*, p. 0533. 2018.

<sup>11</sup> Hodgkinson, John. "History of low-order equivalent systems for aircraft flying qualities." *Journal of Guidance, Control, and Dynamics* 28, no. 4 (2005): 577-583.

---

<sup>12</sup> Morelli, Eugene A., and Vladislav Klein. "Determining the accuracy of maximum likelihood parameter estimates with colored residuals." (1994).

<sup>13</sup> Hakim, T. M. I., & Arifianto, O. (2018, April). Implementation of Dryden Continuous Turbulence Model into Simulink for LSA-02 Flight Test Simulation. In *Journal of Physics: Conference Series* (Vol. 1005, No. 1, p. 012017). IOP Publishing.

<sup>14</sup> Hakim, T. M. I., & Arifianto, O. (2018, April). Implementation of Dryden Continuous Turbulence Model into Simulink for LSA-02 Flight Test Simulation. In *Journal of Physics: Conference Series* (Vol. 1005, No. 1, p. 012017). IOP Publishing.

<sup>15</sup> McRuer, Duane T. "Human pilot dynamics in compensatory systems-theory, models, and

experiments with controlled element and forcing function variations." *AFFDL-TR-65-15*(1965).

<sup>16</sup> Roscoe, A. H., and Ellis, G. A., "A subjective rating scale assessing pilot workload in flight. A decade of practical use. Royal Aerospace Establishment." Technical Report 90019. Farnborough. UK: Royal Aerospace Establishment, 1990.

<sup>17</sup> Bachelder, E., and Aponso, B.: *Novel Estimation of Pilot Performance Characteristics*, AIAA Atmospheric Flight Mechanics Conference, AIAA SciTech Forum, (AIAA 2017-1640).

<sup>18</sup> Bachelder, E., and Aponso, B.: *Novel Estimation of Pilot Performance Characteristics*, AIAA Atmospheric Flight Mechanics Conference, AIAA SciTech Forum, (AIAA 2017-1640).